

Radiative corrections in exclusive semileptonic B -meson decays to (pseudo)scalar final state mesons

Florian Urs Bernlochner^{1,2}, Heiko Lacker^{1,3}

¹ *Department of Physics, Humboldt University of Berlin, Newtonstrasse 15, 12489 Berlin, Germany*

² *florian@slac.stanford.edu*, ³ *lacker@physik.hu-berlin.de*

Abstract:

We present a new tool to study the long-distance radiative corrections to differential and total decay rate predictions of semileptonic B -meson decays into exclusive pseudoscalar final states $B \rightarrow D l \nu$ and $B \rightarrow \pi l \nu$, and the scalar final state $B \rightarrow D_0^* l \nu$. Next-to-leading order corrections are an important aspect in the extraction of the Cabibbo-Kobayashi-Maskawa matrix elements $|V_{cb}|$ and $|V_{ub}|$ at B -factory experiments: virtual and real photons couple to all charged particles of the decay, altering the resulting decay dynamics and enhancing the total decay rate. For $B^0 \rightarrow D^+ l \nu$ the total decay rate is increased by $\delta_{\text{total}} = 2.048(186)\%$ due to next-to-leading order effects. The uncertainties in the parenthesis are the sum of numerical and theoretical uncertainties. This results in a decrease of $|V_{cb}|$ of $-1.009(45)\%$ extracted from such decays. Similarly we find for $B^+ \rightarrow D^0 l \nu$ decays an increase of $\delta_{\text{total}} = 1.031(367)\%$ to the total decay rate, resulting in a decrease of $-0.511(90)\%$ in $|V_{cb}|$. For $B^0 \rightarrow \pi^+ l \nu$ decays, we predict a change of the total rate due to next-to-leading order effects of $\delta_{\text{total}} = 2.404(207)\%$, leading to a decrease of $|V_{ub}|$ of $-1.181(49)\%$ extracted from such decays. Similarly for $B^+ \rightarrow \pi^0 l \nu$ we find an increase of $\delta_{\text{total}} = 1.104(380)\%$ to the total decay rate, resulting into a decrease of $-0.548(92)\%$ of $|V_{ub}|$. For $B^0 \rightarrow D_0^{*+} l \nu$ and $B^+ \rightarrow D_0^{*0} l \nu$ decays, we find an increase of $\delta_{\text{total}} = 2.156(100)\%$ and $\delta_{\text{total}} = 1.144(322)\%$, respectively. This results in a decrease of $-1.061(24)\%$ and $-0.567(80)\%$ of $|V_{cb}|$, respectively.

1. Introduction

In the Standard Model, the Cabibbo-Kobayashi-Maskawa (CKM) matrix [1] governs the weak transitions between the up- and down-type quark generations. The precision determination of its matrix elements and their CP symmetry breaking complex phase in the B -meson sector is the focus of intense research over the past decade. The combination of such measurements to test unitarity of the CKM matrix as a whole is considered a strong instrument for the search of physics beyond the Standard Model [2, 3].

In this paper, we present a calculation and a simulation tool for the electromagnetic one-loop corrections in exclusive semileptonic B -meson decays: $B \rightarrow D l \nu$, $B \rightarrow \pi l \nu$, and $B \rightarrow D_0^* l \nu$. Next-to-leading order corrections to such decays are an important aspect in the extraction of the CKM matrix elements $|V_{cb}|$ and $|V_{ub}|$ at B -factory experiments: virtual and real photons couple to all charged particles of the decay, which alters the resulting decay dynamics and enhances the weak decay rate. To correct for the altered decay dynamics, experimentalists use approximative all-purpose next-to-leading order algorithms. These exploit that such corrections are universal in the soft photon energy limit [4, 5]. In addition, the total leading order decay rate of semileptonic decays are corrected by the known leading logarithm of the virtual corrections at parton level [6, 7].

Experience from exclusive semileptonic K -meson decays illustrate the importance of having a good understanding of such radiative effects: until 2004 the global average of the extracted value of $|V_{us}|$ from K_{l3}^+ and K_{l3}^0 decays implied the violation of CKM unitarity by two standard deviations [8]. Further measurements proofed dissonant with these findings [9, 10, 11, 12], indicating that the achieved experimental precision needed an understanding of electromagnetic corrections at the percent level. Since for many decays next-to-leading order calculations do not exist, experiments often use the approximative all-purpose algorithm PHOTOS [13, 14] to study the reconstruction efficiency and acceptance. The accuracy of this approach was tested by the KTeV collaboration, using the measured photon spectra from radiative K_{l3}^0 decays: the angular distribution of the simulated photons did not agree well with the predicted spectrum [15]. This lead to the development of the next-to-leading order Monte Carlo generator KLOR (see [15]), whose next-to-leading order calculation is based on a phenomenological model. Its predicted angular photon distribution agreed satisfactorily with the measured spectra. Although this approach is very precise, it is also the most complicated to adopt for an experiment: electromagnetic next-to-leading order calculations only exist for a few decay modes. Most of them build on customized Monte Carlo generators, and including their findings is a challenging task. The KLOE collaboration resolved this by using the approach of [16], which goes beyond the soft photon-energy limit of [13, 14] by including the full real-emission matrix elements.

Over the last 10 years an increasing amount of data and a better understanding of detector effects lead to a very accurate picture of physics at both B -factory experiments. This increased precision lead to the demand of knowledge of next-to-leading order electromagnetic effects beyond the precision of approximative all-purpose algorithms. This paper was written to close this important gap and improve the status quo in a twofold way: first by providing a Monte Carlo generator that produces differential decay rates based on a phenomenological next-to-leading order calculation; and second by calculating the unknown isospin breaking phenomenological contributions to the next-to-leading order enhancement of the total decay rate. The latter give small corrections to the leading logarithm at parton level, and therefore to the extracted values of $|V_{cb}|$ and $|V_{ub}|$ from semileptonic decays.

Our model is based on the considerations of [17, 18, 19], that calculate the next-to-leading order effects of semileptonic K_{l3} decays. We improve this Ansatz there by including the decay mode dependent real corrections to the weak decay dynamics. This paper proceeds as follows: Sec. 2 briefly reviews exclusive $B \rightarrow X l \nu$ decays at tree-level. Sec. 3 thereafter develops the next-to-leading order formalism, and presents the corresponding matrix elements. Sec. 4 describes the numerical methods used to integrate the next-to-leading order matrix elements, and Sec. 5 presents the results for the next-to-leading order differential rate predictions and the long-distance correction to total decay rate. Sec. 6 summarizes our result and presents our conclusions.

Note that charge-conjugated modes are implied throughout this paper and that natural units, $c = 1$ and $\hbar = 1$, are used.

2. Phenomenological tree-level decay revised

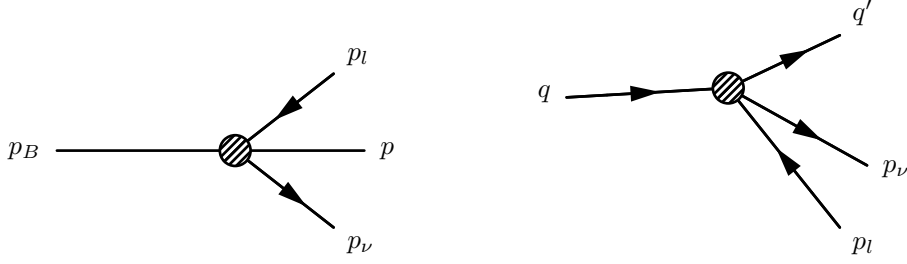


Figure 1: The tree-level weak $B \rightarrow X l \nu$ decay using Fermi theory is shown: on the left hand side within the phenomenological picture, and on the right hand side at parton level within the Standard model. The shaded circle in the transition represents the Fermi vertex.

The phenomenological interaction Lagrangian of a weak $B \rightarrow X l \nu$ decay to a (pseudo)scalar final state in Fermi theory is given by

$$\mathcal{L}_W = \frac{G_F}{\sqrt{2}} V_{xb} \bar{\psi}_\nu \gamma_\mu P_L \psi_l [(f_+ + f_-) \phi \partial^\mu \phi_B + (f_+ - f_-) \phi_B \partial^\mu \phi], \quad (1)$$

where ψ_l and ψ_ν are the Dirac fields of the lepton, respectively, the neutrino, ϕ_B and ϕ are the scalar fields of the initial and final state mesons, G_F the Fermi coupling, V_{xb} the CKM matrix element of the $b \rightarrow x$ transition and $P_L = 1 - \gamma_5$ the left-handed projection operator. This Lagrangian leads to the transition matrix element

$$\mathcal{M}_0^0 = -i \frac{G_F}{\sqrt{2}} V_{xb} \bar{u}(p_\nu) \gamma^\mu P_L v(p_l) H_\mu, \quad (2)$$

with the hadronic current $H_\mu = (p_B + p)_\mu f_+ + (p_B - p)_\mu f_-$. In the following \mathcal{M}_m^n denotes a matrix element at $\mathcal{O}(\alpha^n)$ with m photons in the final state, the tree-level matrix element consequently is indicated as \mathcal{M}_0^0 . The four-momenta in Eqn. (2) are introduced in Fig. 1. The form factors $f_\pm = f_\pm(t)$ describe the weak decay dynamic and are functions of the four-momentum transfer squared of the B -meson to the X -meson system, e.g.

$$t = (p_B - p)^2. \quad (3)$$

The tree-level differential decay rate in the B -meson rest frame is given by

$$d\Gamma_0^0 = \frac{1}{64 \pi^3 m_B} |\mathcal{M}_0^0|^2 dE dE_l, \quad (4)$$

with $E = p^0$ and $E_l = p_l^0$. In the following Γ_m^n denotes the decay rate at $\mathcal{O}(\alpha^n)$ with m photons in the final state, consequently the tree-level decay rate is indicated as Γ_0^0 . The explicit expressions of f_\pm as function of the momentum transfer squared for $B \rightarrow D l \nu$, $B \rightarrow D_0^* l \nu$, and $B \rightarrow \pi l \nu$ decays can be found in App. A.

3. Next-to-leading order corrections

The arising electromagnetic next-to-leading order corrections can be divided into two energy regimes: short-distance corrections at parton level, and long-distance corrections within the phenomenological model. The virtual short-distance corrections were calculated by [6, 7] using a short-distance expansion valid at high energies (such that no leading corrections from strong interactions occur). The relevant tree-level matrix element in this expansion is

$$\mathcal{M}_0^0 = -i \frac{G_F}{\sqrt{2}} V_{xb} \left[\bar{u}(p_\nu) \gamma^\mu P_L v(p_l) \right] \left[\bar{x}(q') \gamma_\mu P_L b(q) \right]. \quad (5)$$

The four-momenta in Eqn. (5) are introduced in Fig. 1. The virtual electroweak corrections in this expansion are

$$\mathcal{M}_0^1 = \mathcal{M}_0^0 \left[1 + \frac{3}{4} \frac{\alpha}{\pi} (1 + 2|\bar{Q}|) \ln \frac{m_Z}{\mu_0} \right] + \dots \quad (6)$$

where $\bar{Q} = \pm \frac{1}{6}$ is the averaged electromagnetic charge of the decaying quark line, α the fine-structure constant, μ_0 a typical energy scale of the interaction, and the ellipses indicate further non-leading terms. The explicit dependency of the large logarithm involving the Z -boson mass originates from including electroweak corrections due to Z -boson exchange. This inclusion renders the arising loop integrals ultraviolet (UV) finite. For semileptonic B -meson decays a reasonable scale is given by the b -quark mass in the $\overline{\text{MS}}$ scheme $m_b = \bar{m}_b(\bar{m}_b)$, therefore $\mu_0 = m_b$. The logarithm in Eqn. (6) represents now the short-distance corrections due to virtual particle exchange ranging from energies between m_b and m_Z . The corresponding virtual long-distance corrections have to be matched to this result, by suppressing (as done e.g. by Pauli-Villars regularization [20]) or by cutting off loop-contributions (e.g. by employing an Euclidian cut-off) above this scale. In this paper we make use of the former regularization approach. These long-distance corrections can be obtained by minimal coupling of the photon field to Eqn. (1) and the free-field Lagrangian of the involved Dirac and (pseudo)scalar fields. The matrix elements of the arising real and virtual next-to-leading order diagrams are presented in the following subsections. Matching the short-distance with the long-distance picture ensures a meaningful value of Fermi's constant: G_F is matched to the Muon decay constant in the short-distance picture.

3.1. Real long-distance next-to-leading order matrix elements

We first focus on the emission from external legs, shown in Fig. 2. Depending on the origin of the emission the four-momentum transfer squared changes: In addition to Eqn. (3) which remains unchanged for emission from the lepton leg, we find the relevant four-momentum transfer squared for hadronic legs to be $t' = (p_B - p - k)^2$, where k is the four-momentum of the emitted photon.

The leptonic emission matrix element is given by

$$\mathcal{M}_1^{\frac{1}{2}} = i e \frac{G_F}{\sqrt{2}} V_{xb} \bar{u}(p_\nu) \gamma^\mu P_L \left(-\frac{\not{\epsilon}^* \not{k}}{2p_l \cdot k + \lambda^2} + \frac{p_l \cdot \epsilon^*}{p_l \cdot k + \frac{1}{2}\lambda^2} \right) v(p_l) H_\mu(p_B, p, t), \quad (7)$$

where $\epsilon^* = \epsilon^*(k)$ denotes the polarization vector of the real final state photon, and the hadronic current $H_\mu(p_B, p, t) = H_\mu$. Similarly the hadronic initial emission is

$$\mathcal{M}_1^{\frac{1}{2}} = i e \frac{G_F}{\sqrt{2}} V_{xb} \bar{u}(p_\nu) \gamma^\mu P_L v(p_l) \left(-\frac{p_B \cdot \epsilon^*}{p_B \cdot k + \frac{1}{2}\lambda^2} \right) H_\mu(p_B - k, p, t'). \quad (8)$$

whereas the hadronic final emission is given by

$$\mathcal{M}_1^{\frac{1}{2}} = i e \frac{G_F}{\sqrt{2}} V_{xb} \bar{u}(p_\nu) \gamma^\mu P_L v(p_l) \left(-\frac{p \cdot \epsilon^*(k)}{p \cdot k + \frac{1}{2}\lambda^2} \right) H_\mu(p_B, p + k, t'). \quad (9)$$

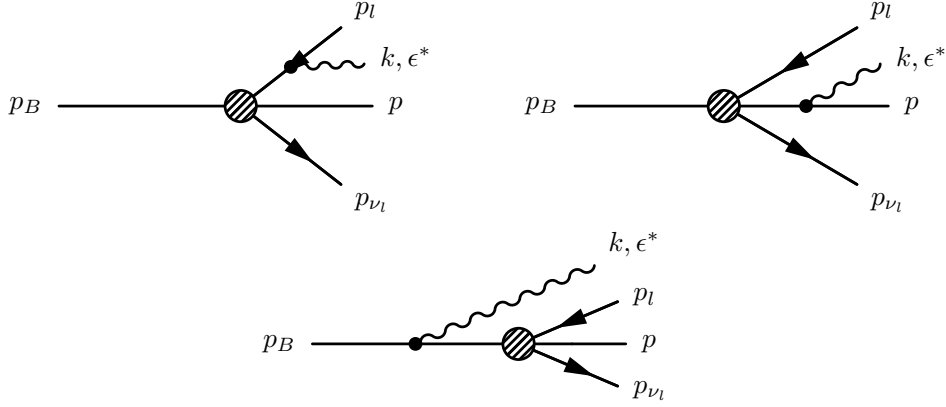


Figure 2: The corresponding Feynman diagrams for the emission of one real photon from all external legs is shown.

Consequently, the hadronic current changes when an emission from a hadronic leg occurs:¹

$$H_\mu(p_B - k, p, t') = (p_B + p - k)_\mu f_+(t') + (p_B - p - k)_\mu f_-(t'), \quad (10)$$

$$H_\mu(p_B, p + k, t') = (p_B + p + k)_\mu f_+(t') + (p_B - p - k)_\mu f_-(t'). \quad (11)$$

The arising collinear and soft-divergencies are regulated by introducing a small, but finite photon mass λ . This is the standard prescription of QED and this artificial parameter cancels exactly with the infrared divergencies of the virtual diagrams. Since we want to evaluate the real and virtual rates separately, the non-vanishing longitudinal polarization has to be taken into account. The polarization vectors of a real photon (in the $(0, 0, 0, 1)$ direction) are thus given by

$$\epsilon_1^*(k) = \frac{1}{\sqrt{2}}(0, 1, i, 0), \quad \epsilon_2^*(k) = \frac{1}{\sqrt{2}}(0, 1, -i, 0), \quad \epsilon_3^*(k) = \frac{1}{\lambda}(\sqrt{k^2 + \lambda^2}, 0, 0, k). \quad (12)$$

Summing all contributions of the legs of a specific mode yields an incomplete picture of the emission process: The resulting summed matrix element is not gauge invariant in the limit of $\lambda \rightarrow 0$ and diverges as $\frac{k^0}{\lambda}$, due to the longitudinal polarization ϵ_3^* . The missing matrix element contribution that restores gauge invariance is given by the vertex emission diagram shown in Fig. 3. It can be obtained in two ways: by minimal coupling of the photon field to Eqn. (1) or by using the Ward-identity of QED [21]. The former is insufficient for emission scenarios of non-matching four-momentum transfers, but yields a good consistency check of the latter procedure, which we will use.

3.1.1. Vertex-emission matrix element via minimal coupling: $t = t'$

Using minimal coupling yields for the scenario of a charged initial state the vertex-emission matrix element

$$\mathcal{M}_1^{\frac{1}{2}} = -i e \frac{G_F}{\sqrt{2}} V_{xb} \bar{u}(p_\nu) P_R \not{\epsilon}^* f_3 v(p_l), \quad (13)$$

with $f_3 = (f_+ + f_-)$ and $P_R = 1 + \gamma_5$ the right-handed projection operator. Similarly, the charged final state scenario vertex-emission matrix element is

$$\mathcal{M}_1^{\frac{1}{2}} = i e \frac{G_F}{\sqrt{2}} V_{xb} \bar{u}(p_\nu) P_R \not{\epsilon}^* f_2 v(p_l), \quad (14)$$

with $f_2 = (f_+ - f_-)$.

¹Although true within the phenomenological model, this is a non-trivial assumption: The altered hadronic current, whose model dependent form is unknown for all decays discussed here, could depend on further kinematic quantities.

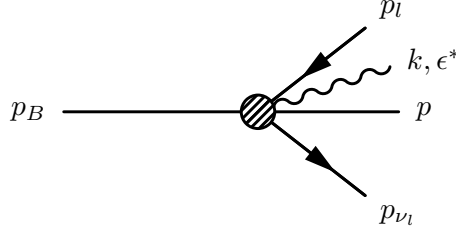


Figure 3: The Feynman diagram of the vertex emission is shown.

3.1.2. Vertex-emission matrix element via Ward-identity: $t = t'$

The Ward identity of QED implies that shifts $\epsilon^* \rightarrow \epsilon^* + \zeta k^\mu$ with $\zeta \in \mathbb{C}$ leave physical amplitudes and consequently matrix elements invariant. It is therefore imperative that

$$\lim_{\lambda \rightarrow 0} \sum \epsilon^{*\mu} \mathcal{M}_\mu \rightarrow \lim_{\lambda \rightarrow 0} \sum k^\mu \mathcal{M}_\mu = 0 \quad (15)$$

is satisfied, where the sum is taken over all diagrams with identical final states. This gives us a recipe to find the missing vertex-emission contributions from the summed emissions of the legs:

Step 1: Sum all matrix elements but the vertex-emission of a particular mode.

Step 2: Apply the Ward-transformation: $\epsilon^* \rightarrow k$.

Step 3: Isolate the gauge-invariance spoiling terms and transform them back via $k \rightarrow \epsilon^*$.

This recipe is the Low-Adler-Dothan procedure [22, 23] and allows to calculate the emission-vertex matrix element for non-matching four-momentum transfers: $t \neq t'$. However *steps 1-3* do not determine uniquely the emission-vertex: the resulting expression might differ by structure dependent contributions. The impact of such terms was studied in [24, 25], finding negligible to small numerical impact on the resulting differential and total rates. We first rederive the minimal coupling results by setting $t = t'$ and sum the matrix elements of Eqns. (7) and (8). Following all steps we find for the charged initial state vertex-emission matrix element,

$$\mathcal{M}_1^{\frac{1}{2}} = -i e \frac{G_F}{\sqrt{2}} V_{\text{xb}} \bar{u}(p_\nu) P_R \not{\epsilon}^* f_3(t) v(p_l), \quad (16)$$

which is consistent with Eqn. (13). Similarly, we find by summing Eqns. (7) and (9) for the charged final state vertex-emission matrix element,

$$\mathcal{M}_1^{\frac{1}{2}} = i e \frac{G_F}{\sqrt{2}} V_{\text{xb}} \bar{u}(p_\nu) P_R f_2(t) \not{\epsilon}^* v(p_l), \quad (17)$$

which is consistent with Eqn. (14).

3.1.3. Vertex-emission matrix element via Ward-identity: $t \neq t'$

The hadronic currents that appear in the hadronic emission matrix elements Eqns. (8) and (9) separate as

$$H_\mu(p_B - k, p, t') = H_\mu(p_B, p, t') - f_3(t')(k)_\mu, \quad (18)$$

$$H_\mu(p_B, p + k, t') = H_\mu(p_B, p, t') + f_2(t')(k)_\mu. \quad (19)$$

Expanding the form factors f_\pm in a Taylor series about $k = 0$ yields

$$f_\pm(t') = f_\pm(t) + Z_{f_\pm}(t, k) = f_\pm(t) + k_\alpha Z_{f_\pm}^\alpha(t, k), \quad (20)$$

where $Z_{f_{\pm}}(t, k)$ denote the summed Taylor coefficients up to a specific, but arbitrary order. Inserting Eqn. (20) into Eqns. (18) and (19) yields

$$H_{\mu}(p_B - k, p, t') = \left[H_{\mu} - f_3(t)(k)_{\mu} \right] + (p_B + p - k)_{\mu} Z_{f_+}(t, k) + (p_B - p - k)_{\mu} Z_{f_-}(t, k), \quad (21)$$

and

$$H_{\mu}(p_B, p + k, t') = \left[H_{\mu} + f_2(t)(k)_{\mu} \right] + (p_B + p + k)_{\mu} Z_{f_+}(t, k) + (p_B - p - k)_{\mu} Z_{f_-}(t, k), \quad (22)$$

respectively. Using $p_B - k = p + p_l + p_{\nu}$, employing the Dirac equation and following the Low-Adler-Dothan prescription yields for the vertex-emission matrix element of the charged initial state,

$$\mathcal{M}_1^{\frac{1}{2}} = i e \frac{G_F}{\sqrt{2}} V_{xb} [\bar{u}(p_{\nu}) P_R] \left(-f_3(t) \not{\epsilon}^* + (2\not{p} + m_l) \epsilon_{\alpha}^* Z_{f_+}^{\alpha}(t, k) + (m_l) \epsilon_{\alpha}^* Z_{f_-}^{\alpha}(t, k) \right) v(p_l). \quad (23)$$

Similarly one finds for the vertex-emission matrix element of the charged final state,

$$\mathcal{M}_1^{\frac{1}{2}} = i e \frac{G_F}{\sqrt{2}} V_{xb} [\bar{u}(p_{\nu}) P_R] \left(f_2(t) \not{\epsilon}^* + (2\not{p}_B - m_l) \epsilon_{\alpha}^* Z_{f_+}^{\alpha}(t, k) + (m_l) \epsilon_{\alpha}^* Z_{f_-}^{\alpha}(t, k) \right) v(p_l). \quad (24)$$

The explicit expressions of $Z_{f_{\pm}}$ for $B \rightarrow D l \nu$, $B \rightarrow D_0^* l \nu$, and $B \rightarrow \pi l \nu$ form factors can be found in App. B.

3.2. Virtual long-distance next-to-leading order corrections

In this section the matrix elements of all virtual long-distance loop-diagrams will be presented. We work in the on-shell renormalization scheme, where all the bare particle masses of the free phenomenological Lagrangian are matched to the corresponding pole-masses of their propagators. In addition we treat the arising loop-integrals in $D = 4 - 2\epsilon$ dimensions. We use the standard notation introduced by Passarino and Veltman [26] and express the loop-integrals as A , B and C functions. This is further explained in App. C. The resulting virtual matrix elements can be transformed from dimensional regularization into Pauli-Villars regularization employing a simple set of replacements and adding counter-terms.

The arising virtual corrections separate into three classes: wave-function renormalization of external legs, inter-particle exchange diagrams and coupling to the vertex. In the two latter cases the explicit k -dependency on the four-momentum transfer squared t is neglected and assumed to have negligible impact on the loop-integration. This is indicated by writing t_c instead of t in the relevant expressions.

3.2.1. Wave-function renormalization

Fig. 4 summarizes all relevant contributions of the wave-function renormalization. The fermionic wave-function renormalization factor is given by

$$\frac{1}{2} \frac{d\Sigma(\not{p}_l)}{d\not{p}_l} = \frac{1}{2} \frac{\alpha}{4\pi} \left[1 + 2B_1(p_l^2; m_l^2, \lambda^2) + 4m_l^2 \dot{B}_1(p_l^2; m_l^2, \lambda^2) + 8m_l^2 \dot{B}_0(p_l^2; m_l^2, \lambda^2) \right], \quad (25)$$

where $\Sigma(\not{p}_l)$ is the fermionic self-energy correction. Similarly one finds for the charged initial pseudoscalar leg a wave-function renormalization factor of

$$\frac{1}{2} \frac{d\Sigma}{dp^2} = \frac{1}{2} \frac{\alpha}{4\pi} \left[2B_0(p^2; m^2, \lambda^2) + (4m^2 - \lambda^2) \dot{B}_0(p^2; m^2, \lambda^2) \right], \quad (26)$$

whereas for the charged (pseudo)scalar final state leg we find

$$\frac{1}{2} \frac{d\Sigma}{dp_B^2} = \frac{1}{2} \frac{\alpha}{4\pi} \left[2B_0(p_B^2; m_B^2, \lambda^2) + (4m_B^2 - \lambda^2) \dot{B}_0(p_B^2; m_B^2, \lambda^2) \right], \quad (27)$$

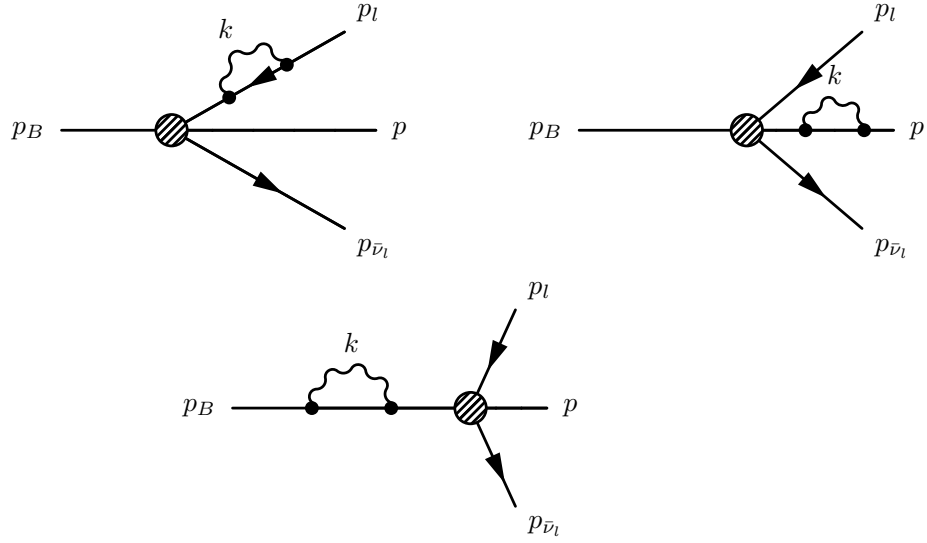


Figure 4: The corresponding Feynman diagrams of the arising self-energy correction of the charged anti-fermion final, the charged pseudoscalar initial, and the charged (pseudo)scalar final state mesons are shown.

with Σ the scalar self-energy. The total correction due wave-function renormalization is then given by

$$\mathcal{M}_0^1 = \frac{1}{2} \left[\frac{d\Sigma(p_l)}{dp_l} + \frac{d\Sigma}{dp^2} \right] \mathcal{M}_0^0, \quad (28)$$

or

$$\mathcal{M}_0^1 = \frac{1}{2} \left[\frac{d\Sigma(p_l)}{dp_l} + \frac{d\Sigma}{dp_B^2} \right] \mathcal{M}_0^0, \quad (29)$$

depending on the decay mode.

3.2.2. Inter-particle exchange diagrams

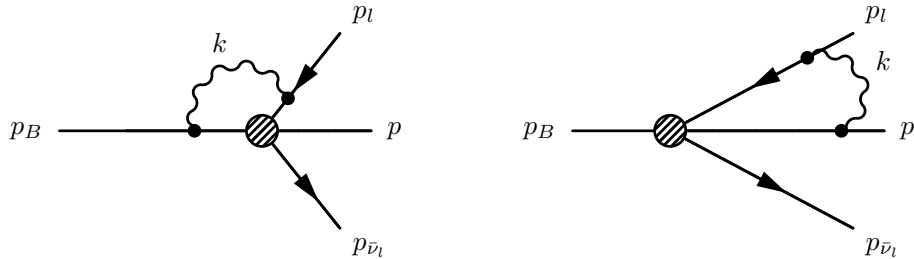


Figure 5: The corresponding Feynman diagrams of the arising inter-particle photon exchange diagram between the charged lepton leg and the charged initial or final state mesons are shown.

Fig. 5 summarizes the two relevant photon exchange diagrams. The inter-particle photon exchange diagram between the charged lepton leg and the charged pseudoscalar initial state is given by

$$\mathcal{M}_0^1 = (+e^2) \frac{1}{\sqrt{2}} G_F V_{xb} [\bar{u}(p_\nu) P_R \gamma_\mu \Gamma^\mu v(p_l)]. \quad (30)$$

with the correction tensor Γ^μ :

$$\begin{aligned} \Gamma^\mu &= \frac{i}{(4\pi)^2} \left[H^\mu \left(-4(p_B \cdot p_l) \right) \right] C_0(p_l^2, s, p_B^2; \lambda^2, m_l^2, m_B^2) \\ &\quad - \frac{i}{(4\pi)^2} \left[\left(f_3(t_c) p_l^\mu \right) (4p_B \cdot p_l) + (H^\mu) \left(4p_B \cdot p_l + 2m_l^2 - 2p_B \not{p}_l \right) \right] C_1(p_l^2, s, p_B^2; \lambda^2, m_l^2, m_B^2) \\ &\quad - \frac{i}{(4\pi)^2} \left[\left(f_3(t_c) p_B^\mu \right) (4p_B \cdot p_l) + (H^\mu) \left(2p_B \cdot p_l + 2m_B^2 \right) \right] C_2(p_l^2, s, p_B^2; \lambda^2, m_l^2, m_B^2) \\ &\quad + \frac{i}{(4\pi)^2} \left[\left(-f_3(t_c) p_l^\mu \right) \left(4p_B \cdot p_l + 2m_l^2 - 2p_B \not{p}_l \right) \right] C_{11}(p_l^2, s, p_B^2; \lambda^2, m_l^2, m_B^2) \\ &\quad + \frac{i}{(4\pi)^2} \left[\left(-f_3(t_c) p_B^\mu \right) \left(2p_B \cdot p_l + 2m_B^2 \right) \right] C_{22}(p_l^2, s, p_B^2; \lambda^2, m_l^2, m_B^2) \\ &\quad + \frac{i}{(4\pi)^2} \left[\left(-f_3(t_c) p_l^\mu \right) \left(2p_B \cdot p_l + 2m_B^2 \right) \right. \\ &\quad \quad \left. + \left(-f_3(t_c) p_B^\mu \right) \left(4p_B \cdot p_l + 2m_l^2 - 2p_B \not{p}_l \right) \right] C_{12}(p_l^2, s, p_B^2; \lambda^2, m_l^2, m_B^2) \\ &\quad + \frac{i}{(4\pi)^2} \left[\left(-f_3(t_c) \right) \left(2p_l^\mu + 2\gamma^\mu \not{p}_B \right) \right] C_{00}(p_l^2, s, p_B^2; \lambda^2, m_l^2, m_B^2) \\ &\quad + \frac{i}{(4\pi)^2} \left[-H^\mu + f_3(t_c) p_l^\mu \right] B_0(s; m_l^2, m_B^2) + \frac{i}{(4\pi)^2} \left[f_3(t_c) (p_l - p_B)^\mu \right] B_1(s; m_l^2, m_B^2), \quad (31) \end{aligned}$$

where $s = (p_l - p_B)^2$. Similarly we find for the correction tensor Γ^μ of the inter-particle photon exchange diagram between the charged lepton leg and the charged (pseudo)scalar final state the expression:

$$\begin{aligned} \Gamma^\mu &= -\frac{i}{(4\pi)^2} \left[H^\mu \left(-4(p \cdot p_l) \right) \right] C_0(p_l^2, s, p^2; \lambda^2, m_l^2, m^2) \\ &\quad + \frac{i}{(4\pi)^2} \left[\left(f_2(t_c) p_l^\mu \right) (-4p \cdot p_l) + (H^\mu) \left(4p \cdot p_l - 2m_l^2 - 2p \not{p}_l \right) \right] C_1(p_l^2, s, p^2; \lambda^2, m_l^2, m^2) \\ &\quad - \frac{i}{(4\pi)^2} \left[\left(f_2(t_c) p^\mu \right) (-4p \cdot p_l) + (H^\mu) \left(2m^2 - 2p \cdot p_l \right) \right] C_2(p_l^2, s, p^2; \lambda^2, m_l^2, m^2) \\ &\quad - \frac{i}{(4\pi)^2} \left[\left(f_2(t_c) p_l^\mu \right) \left(4p \cdot p_l - 2m_l^2 - 2p \not{p}_l \right) \right] C_{11}(p_l^2, s, p^2; \lambda^2, m_l^2, m^2) \\ &\quad - \frac{i}{(4\pi)^2} \left[\left(f_2(t_c) p^\mu \right) \left(2m^2 - 2p \cdot p_l \right) \right] C_{22}(p_l^2, s, p^2; \lambda^2, m_l^2, m^2) \\ &\quad + \frac{i}{(4\pi)^2} \left[\left(f_2(t_c) p_l^\mu \right) \left(2m^2 - 2p \cdot p_l \right) \right. \\ &\quad \quad \left. + \left(f_2(t_c) p^\mu \right) \left(4p \cdot p_l - 2m_l^2 - 2p \not{p}_l \right) \right] C_{12}(p_l^2, s, p^2; \lambda^2, m_l^2, m^2) \\ &\quad - \frac{i}{(4\pi)^2} \left[\left(f_2(t_c) \right) \left(-2p_l^\mu + 2\gamma^\mu \not{p} \right) \right] C_{00}(p_l^2, s, p^2; \lambda^2, m_l^2, m^2) \\ &\quad - \frac{i}{(4\pi)^2} \left[H^\mu + f_2(t_c) p_l^\mu \right] B_0(s; m_l^2, m^2) + \frac{i}{(4\pi)^2} \left[f_2(t_c) (p_l + p)^\mu \right] B_1(s; m_l^2, m^2), \quad (32) \end{aligned}$$

where $s = (p_l + p)^2$.

3.2.3. Virtual vertex diagrams

Fig. 6 summarizes the relevant three diagrams involving the loops of the Fermi vertex to the charged legs, where we neglect the small corrections due to vertex-vertex loops. By using the vertex-couplings in

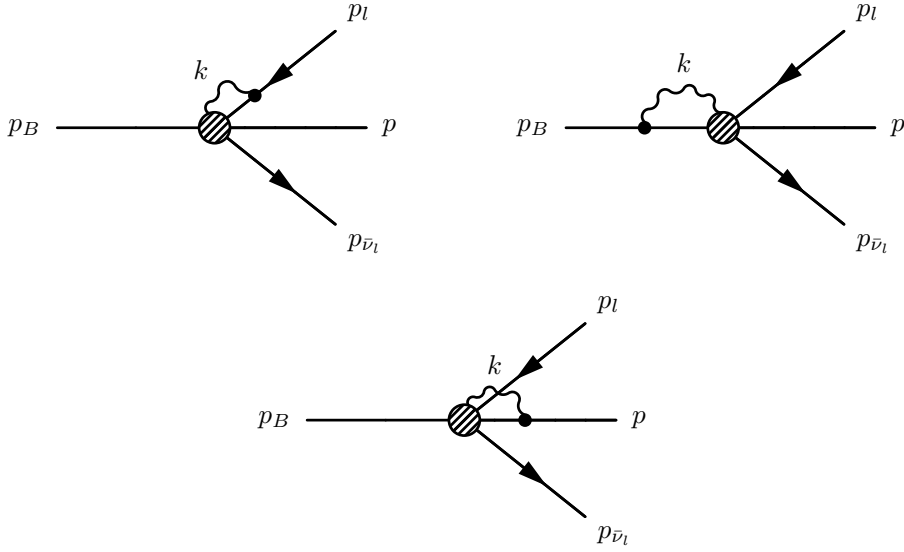


Figure 6: The Feynman diagrams of the loop corrections from the charged vertex of the charged pseudoscalar initial state mode, respectively, the charged (pseudo)scalar final state mode, to the charged particles of a particular decay mode are shown.

Eqn. (13) the summed vertex loops of the decay mode with a charged pseudoscalar hadron in the initial state we find the matrix element

$$\mathcal{M}_0^1 = (e^2) \frac{G_F}{\sqrt{2}} V_{xb} [\bar{u}(p_\nu) P_R \Lambda v(p_l)], \quad (33)$$

with the correction matrix Λ :

$$\begin{aligned} \Lambda = & \frac{i}{(4\pi)^2} [2\not{p}_l f_3(t_c)] B_0(m_l^2; \lambda^2, m_l^2) + \frac{i}{(4\pi)^2} [2\not{p}_B f_3(t_c)] B_0(m_B^2; \lambda^2, m_B^2) \\ & + \frac{i}{(4\pi)^2} \frac{1}{m_l^2} [\not{p}_l f_3(t_c)] A_0(m_l^2) + \frac{i}{(4\pi)^2} \frac{1}{2m_B^2} [-\not{p}_B f_3(t_c)] A_0(m_B^2) \\ & + \frac{i}{(4\pi)^2} [\not{p}_l f_3(t_c)]. \end{aligned} \quad (34)$$

Similarly, one finds with Eqn. (14) for the decay mode with a charged (pseudo)scalar hadron in the final state the correction matrix

$$\begin{aligned} \Lambda = & \frac{i}{(4\pi)^2} [-2\not{p}_l f_2(t_c)] B_0(m_l^2; \lambda^2, m_l^2) + \frac{i}{(4\pi)^2} [2\not{p} f_2(t_c)] B_0(m^2; \lambda^2, m^2) \\ & + \frac{i}{(4\pi)^2} \frac{1}{m_l^2} [-\not{p}_l f_2(t_c)] A_0(m_l^2) + \frac{i}{(4\pi)^2} \frac{1}{2m^2} [-\not{p} f_2(t_c)] A_0(m^2) \\ & + \frac{i}{(4\pi)^2} [\not{p}_l f_2(t_c)]. \end{aligned} \quad (35)$$

3.3. Pauli-Villars regularization

In this section the Pauli-Villars replacement rules and counter-terms for the dimensional regularized loop-integrals are stated. Note that in the resulting expressions all explicit dependency on the dimensional

regulator ϵ cancel. The Pauli-Villars approach introduces a massive photon field to the phenomenological Lagrangian by adding

$$\mathcal{L}_{\text{PV}} = \frac{1}{4}\tilde{F}^2 - \mu_0^2 \tilde{A}^2. \quad (36)$$

Minimal coupling of this massive photon to the weak interaction Lagrangian and the free-field terms renders the stated loop-integrals finite and yields the desired regularization as a function of the mass parameter μ_0 . Taking the limit $\mu_0 \rightarrow \infty$ (which is equal to decoupling the Pauli-Villars photon from the rest of the theory) gives rise to a UV divergency growing as $\sim \ln \mu_0^2$. This results in the desired opposite behavior to the short-distance logarithm and suppresses the exchange of virtual particles with energies larger than μ_0 . To match this with the short-distance result Eqn. (6) we fix $\mu_0 = m_b$.

3.3.1. Wave function renormalization

The replacement rules for the fermionic wave-function Eqn. (25) renormalization are given by

$$\begin{aligned} B_0(m_l^2, m_l^2, \lambda^2) &\rightarrow B_0(m_l^2; m_l^2, \lambda^2) - B_0(m_l^2; m_l^2, \mu_0^2), \\ \dot{B}_i(m_l^2, m_l^2, \lambda^2) &\rightarrow \dot{B}_i(m_l^2, m_l^2, \lambda^2) - \dot{B}_i(m_l^2, m_l^2, \mu_0^2), \end{aligned} \quad (37)$$

with $i = 0, 1$. In addition, one needs to add a counter-term:

$$\frac{d\Sigma(\not{p}_l)_{\text{PV terms}}}{d\not{p}_l} = -\frac{\alpha}{4\pi}. \quad (38)$$

Similarly one finds for the charged (pseudo)scalar final state meson wave-function renormalization Eqn. (26) the replacement rule

$$\begin{aligned} B_0(m^2, m^2, \lambda^2) &\rightarrow B_0(m^2; m^2, \lambda^2) - B_0(m^2; m^2, \mu_0^2), \\ \dot{B}_0(m^2, m^2, \lambda^2) &\rightarrow \dot{B}_0(m^2, m^2, \lambda^2) - \dot{B}_0(m^2, m^2, \mu_0^2), \end{aligned} \quad (39)$$

with a counter-term

$$\frac{d\Sigma(p^2)_{\text{PV terms}}}{dp^2} = \frac{\alpha}{4\pi} \left[\mu_0^2 \dot{B}_0(m^2, m^2, \mu_0^2) \right]. \quad (40)$$

The replacement rules and counter-term for the charged initial state can be obtained directly from Eqns. (39) and (40) by replacing $m^2 \rightarrow m_B^2$,

3.3.2. Inter-particle exchange diagrams

For the inter-particle photon exchange diagram between the charged lepton leg and the charged initial pseudoscalar meson leg one finds the following replacement rules for Eqn. (31):

$$\begin{aligned} C_i(p_l^2, s, p_B^2; \lambda^2, m_l^2, m_B^2) &\rightarrow C_i(p_l^2, s, p_B^2; \lambda^2, m_l^2, m_B^2) - C_i(p_l^2, s, p_B^2; \mu_0^2, m_l^2, m_B^2), \\ C_{ij}(p_l^2, s, p_B^2; \lambda^2, m_l^2, m_B^2) &\rightarrow C_{ij}(p_l^2, s, p_B^2; \lambda^2, m_l^2, m_B^2) - C_{ij}(p_l^2, s, p_B^2; \mu_0^2, m_l^2, m_B^2), \\ B_i(s; m_l^2, m_B^2) &\rightarrow 0, \end{aligned} \quad (41)$$

with $i, j = 0, 1, 2$. In addition one must add the counter-terms

$$\begin{aligned} \Gamma_{\text{PV terms}}^\mu &= -\frac{i}{(4\pi)^2} \left[H^\mu \mu_0^2 \right] C_0(p_l^2, s, p_B^2; \mu_0^2, m_l^2, m_B^2) \\ &\quad + \frac{i}{(4\pi)^2} \left[f_3(t_c) (p_l)^\mu \mu_0^2 \right] C_1(p_l^2, s, p_B^2; \mu_0^2, m_l^2, m_B^2) \\ &\quad + \frac{i}{(4\pi)^2} \left[f_3(t_c) (p_B)^\mu \mu_0^2 \right] C_2(p_l^2, s, p_B^2; \mu_0^2, m_l^2, m_B^2). \end{aligned} \quad (42)$$

Similarly for the charged final state meson case of Eqn. (32) it is:

$$\begin{aligned}
C_i(p_l^2, s, p^2; \lambda^2, m_l^2, m^2) &\rightarrow C_i(p_l^2, s, p^2; \lambda^2, m_l^2, m^2) - C_i(p_l^2, s, p^2; \mu_0^2, m_l^2, m^2), \\
C_{ij}(p_l^2, s, p^2; \lambda^2, m_l^2, m^2) &\rightarrow C_{ij}(p_l^2, s, p^2; \lambda^2, m_l^2, m^2) - C_{ij}(p_l^2, s, p^2; \mu_0^2, m_l^2, m^2), \\
B_i(s; m_l^2, m^2) &\rightarrow 0,
\end{aligned} \tag{43}$$

with $i, j = 0, 1, 2$ and the corresponding counter-terms

$$\begin{aligned}
\Gamma_{\text{PV terms}}^\mu &= \frac{i}{(4\pi)^2} \left[H^\mu \mu_0^2 \right] C_0(p_l^2, s, p^2; \mu_0^2, m_l^2, m_B^2) \\
&\quad - \frac{i}{(4\pi)^2} \left[f_2(t_c) (p_l)^\mu \mu_0^2 \right] C_1(p_l^2, s, p^2; \mu_0^2, m_l^2, m^2) \\
&\quad + \frac{i}{(4\pi)^2} \left[f_2(t_c) (p)^\mu \mu_0^2 \right] C_2(p_l^2, s, p^2; \mu_0^2, m_l^2, m^2).
\end{aligned} \tag{44}$$

3.3.3. Virtual vertex diagrams

For the vertex loops of the decay mode with a charged pseudoscalar meson in the initial state Eqn. (34) one finds the replacement rules to be:

$$\begin{aligned}
B_i(m_l^2; \lambda^2, m_l^2) &\rightarrow B_i(m_l^2; \lambda^2, m_l^2) - B_i(m_l^2; \mu_0^2, m_l^2), \\
B_i(m_B^2; \lambda^2, m_B^2) &\rightarrow B_i(m_B^2; \lambda^2, m_B^2) - B_i(m_B^2; \mu_0^2, m_B^2),
\end{aligned} \tag{45}$$

with $i = 0, 1$, and the counter term

$$\Lambda_{\text{PV terms}} = -\frac{i}{(4\pi)^2} \left[\not{p}_l f_3(t_c) \right]. \tag{46}$$

Similarly, for the charge (pseudo)scalar final state meson case Eqn. (35) one finds:

$$\begin{aligned}
B_i(m_l^2; \lambda^2, m_l^2) &\rightarrow B_i(m_l^2; \lambda^2, m_l^2) - B_i(m_l^2; \mu_0^2, m_l^2), \\
B_i(m^2; \lambda^2, m^2) &\rightarrow B_i(m^2; \lambda^2, m^2) - B_i(m^2; \mu_0^2, m^2),
\end{aligned} \tag{47}$$

with $i = 0, 1$, and the counter term

$$\Lambda_{\text{PV terms}} = -\frac{i}{(4\pi)^2} \left[\not{p}_l f_2(t_c) \right]. \tag{48}$$

3.4. Next-to-leading order differential and total rate

Summing now all virtual corrections for a particular mode, that is either Eqns. (30), (28) or (28), (33), and the short-distance enhancement Eqn. (6), yields the virtual next-to-leading order differential rate:

$$d\Gamma_0^0 + d\Gamma_0^1 = \frac{1}{64 \pi^3 m_B} \left(|\mathcal{M}_0^0|^2 + 2 \sum \mathcal{M}_0^0 \mathcal{M}_0^1 + 2 |\mathcal{M}_0^0|^2 \left[\frac{3}{4} \frac{\alpha}{\pi} (1 + 2|\bar{Q}|) \ln \frac{m_Z}{\mu_0} \right] \right) dE dE_l. \tag{49}$$

Similarly one finds for the real corrections by summing all real corrections contributing to a particular mode, that is either Eqns. (7), (8), and (23) or Eqns. (7), (9), and (24), the real next-to-leading order differential rate,

$$d\Gamma_1^{\frac{1}{2}} = \frac{1}{(2\pi)^{12} E E_l E_\nu E_k} \delta^{(4)}(m_B - p - p_l - p_\nu - k) \left| \sum \mathcal{M}_1^{\frac{1}{2}} \right|^2 d^3p d^3p_l d^3p_\nu d^3k, \tag{50}$$

with $E_k = k^0$ and $E_\nu = p_\nu^0$. Integrating Eqns. (49) and (50) yields the next-to-leading order total decay rate. Comparing with the total tree-level decay rate, the integral over phase-space of Eqn. (4), yields the long-distance enhancement factor δ_{LD} due to next-to-leading order effects. It is

$$\Gamma_0^0 + \Gamma_0^1 + \Gamma_1^{\frac{1}{2}} = \left(1 + \delta_{\text{SD}} + \delta_{\text{LD}} \right) \Gamma_0^0, \tag{51}$$

with $\delta_{\text{SD}} = \frac{2\alpha}{\pi} \ln \frac{m_Z}{m_b}$ from Eqn. (6).

4. Numerical evaluation

In order to evaluate Eqns. (49) and (50), we developed the Monte Carlo generator **BLOR** (*B-meson leading order radiative corrections*), which is derived from the code of **KLOR** (*Kaon leading order radiative corrections* - written by Troy Andre [15]). It incorporates all form-factor models of App. A and the complete next-to-leading order matrix elements derived in the previous section. The loop-integrals are evaluated numerically using the software package **Looptools** [27]. For the regularization procedure we can choose between dimensional regularization, Pauli-Villars and an approximative Euclidian cut-off integration. The phase-space integration occurs in two steps: the total tree-level and next-to-leading order rates are calculated to determine δ_{LD} and the radiative fraction

$$\frac{\Gamma_0^0 + \Gamma_0^1}{\Gamma_1^{\frac{1}{2}}}. \quad (52)$$

This is done using the VEGAS algorithm described in [28]. Thereafter the radiative fraction Eqn. (52) is used to mix events generated from the real and virtual next-to-leading order matrix elements using Monte Carlo techniques. In order to optimize the event generation procedure, we use moderately pre-tuned probability density functions of the integration variables in question. In addition to the implemented next-to-leading order calculations, the **BLOR** Monte Carlo generator is interfaced with the approximative next-to-leading order algorithm **PHOTOS** [13, 14]. The code of **BLOR** is publicly accessible and can be found at [29]. The particle masses and couplings employed in the code are summarized in Table 1.

Parameter	Value
m_e GeV/ c^2	0.000510998903
m_μ GeV/ c^2	0.1056583568
m_{B^+} GeV/ c^2	5.27913
m_{B^0} GeV/ c^2	5.27950
m_{D^+} GeV/ c^2	1.86950
m_{D^0} GeV/ c^2	1.86484
m_{π^+} GeV/ c^2	0.13957018
m_{π^0} GeV/ c^2	0.1349766
$m_{D_0^{*+}}$ GeV/ c^2	2.403
$m_{D_0^{*0}}$ GeV/ c^2	2.352
$\bar{m}_b(\bar{m}_b)$ GeV/ c^2	4.2
λ GeV/ c^2	10^{-7}
α -	0.00729735039
G_F ($\hbar c$) ³ GeV ⁻²	$1.166391 \cdot 10^{-5}$

Table 1: Particle masses and couplings employed in the phenomenological Lagrangian. All values are taken from [30]. The b -quark mass is in the $\overline{\text{MS}}$ scheme.

5. Predictions

In the following we quote the values of δ_{LD} calculated from our next-to-leading order model and assess the theoretical uncertainty. Thereafter, we present the normalized kinematical distributions for the final state, lepton meson, and photon. For a complete summary of our findings including comparison with the algorithms of PHOTOS and PHOTONS++ [31], we refer the reader to [32].

5.1. Predictions for δ_{LD}

Uncertainties to our next-to-leading order corrections come from three sources: the numerical evaluation, the neglect of next-to-next-to-leading order and higher diagrams, and the matching procedure. The total integration error of δ_{LD} is given by

$$\sigma_{\text{numerical}} = \left(\sum_{i=1}^m \frac{1}{\sigma_i^2} \right)^{-\frac{1}{2}}, \quad (53)$$

where σ_i is the error of the i th VEGAS evaluation, and m the number of total evaluation steps. The effect of long-distance next-to-next-to-leading and higher order diagrams is estimated by assuming corrections of the same order of magnitude as the next-to-leading order short- and long-distance corrections,

$$\sigma_{\text{nnlo}} = \alpha \left(\delta_{\text{SD}} + \delta_{\text{LD}} \right). \quad (54)$$

The uncertainty, which originates from matching the short-distance with the long-distance picture, is estimated by varying the matching scale μ_0 in the range of $\frac{1}{2}m_b$ and $2m_b$. The resulting averaged difference to δ_{LD} at $\mu_0 = m_b$ is taken as the matching uncertainty:

$$\begin{aligned} \sigma_{\text{matching}} = & \frac{1}{2} \left| \delta_{\text{total}}(\mu_0 = m_b) - \delta_{\text{total}}(\mu_0 = \frac{1}{2}m_b) \right| \\ & + \frac{1}{2} \left| \delta_{\text{total}}(\mu_0 = m_b) - \delta_{\text{total}}(\mu_0 = 2m_b) \right|, \end{aligned} \quad (55)$$

with $\delta_{\text{total}} = \delta_{\text{SD}} + \delta_{\text{LD}}$. The results of these variations for all decay modes are summarized in Tables 2, 3, and 4. Assuming no correlations between the errors the total uncertainty is given by

$$\sigma_{\text{total}}^2 = \sigma_{\text{numerical}}^2 + \sigma_{\text{nnlo}}^2 + \sigma_{\text{matching}}^2. \quad (56)$$

Our predictions for $1 + \delta_{\text{SD}} + \delta_{\text{LD}}$ and $\sqrt{1 + \delta_{\text{SD}} + \delta_{\text{LD}}}$ for $B \rightarrow D l \nu$, $B \rightarrow \pi l \nu$, and $B \rightarrow D_0^* l \nu$ are stated in Table 5. The inverse of the latter is the relevant correction to the CKM matrix elements $|V_{\text{cb}}|$ and $|V_{\text{ub}}|$ gained from measurements. The source of the dominant uncertainty originates from the matching of the phenomenological model with the short-distance calculation. The predicted corrections from short- and long-distance enhancements break the isospin symmetry of the semileptonic decay process, hence the dominant virtual correction Eqn. (30) scales with the mass of the involved charged meson.

5.1.1. Corrections to $|V_{\text{cb}}|$ and $|V_{\text{ub}}|$

The lepton mass has only a negligible effect on the value of the total decay rate. One can therefore assume that

$$\Gamma_0^0(B^+ \rightarrow X^0 e \nu) = \Gamma_0^0(B^+ \rightarrow X^0 \mu \nu) \quad \text{and} \quad \Gamma_0^0(B^0 \rightarrow X^+ e \nu) = \Gamma_0^0(B^0 \rightarrow X^+ \mu \nu), \quad (57)$$

and average the results of $1 + \delta_{\text{SD}} + \delta_{\text{LD}}$ and $\sqrt{1 + \delta_{\text{SD}} + \delta_{\text{LD}}}$ in Table 5 from both lepton channels to decrease the numerical uncertainty of the integration. The matching and next-to-next-to leading order uncertainties then are correlated by 100%. This yields an averaged correction of 2.048(186)% to the total $B^0 \rightarrow D^+ l \nu$ decay rate. The increased total decay rate translates into a decrease of the extracted value of $|V_{\text{cb}}|$ from measurements by $-1.009(45)\%$. Similarly, the $B^+ \rightarrow D^0 l \nu$ total decay rate increases by 1.031(367)%, translating into a decrease of $-0.511(90)\%$ of $|V_{\text{cb}}|$.

Analyses often study B -mesons from the decay chain $\Upsilon(4S) \rightarrow B \bar{B}$ with B either B^+ or B^0 . In order to reduce the statistical uncertainty, and assuming isospin, the $B^+ \rightarrow D^0 l \nu$ and $B^0 \rightarrow D^+ l \nu$ decay rates can be combined. At tree-level this combined total decay rate is given by

$$\Gamma_0^0(B \rightarrow D l \nu) = f_{+-} \Gamma_0^0(B^+ \rightarrow D^0 l \nu) + f_{00} \Gamma_0^0(B^0 \rightarrow D^+ l \nu), \quad (58)$$

with

$$f_{+-} = \mathcal{BF}(\Upsilon(4S) \rightarrow B^+ B^-) \quad \text{and} \quad f_{00} = \mathcal{BF}(\Upsilon(4S) \rightarrow B^0 \bar{B}^0), \quad (59)$$

the branching fractions of the $\Upsilon(4S)$ resonance either decaying into a $B^+ B^-$ or $B^0 \bar{B}^0$ pair. Including the isospin conserving short-distance correction Eqn. (6) yields

$$(1 + \delta_{\text{SD}}) \Gamma_0^0(B \rightarrow D l \nu) \propto |V_{\text{cb}}|^2, \quad (60)$$

with $\delta_{\text{SD}} = 1.430\%$, resulting in a correction of -0.707% to the extracted value of $|V_{\text{cb}}|$. Including the isospin breaking contributions from the long-distance corrections of Table 5 results in

$$(1 + \delta_{\text{SD}} + \delta_{\text{LD}}^+) f_{+-} \Gamma_0^0(B^+ \rightarrow D^0 l \nu) + (1 + \delta_{\text{SD}} + \delta_{\text{LD}}^0) f_{00} \Gamma_0^0(B^0 \rightarrow D^+ l \nu) \propto |V_{\text{cb}}|^2, \quad (61)$$

where δ_{LD}^+ and δ_{LD}^0 either denote the long-distance next-to-leading order correction of $B^+ \rightarrow D^0 l \nu$ or $B^0 \rightarrow D^+ l \nu$ decays. The total correction is

$$(1 + \delta_{\text{total}}) \Gamma_0^0(B \rightarrow D l \nu) \propto |V_{\text{cb}}|^2, \quad (62)$$

with

$$\delta_{\text{total}} = (\delta_{\text{SD}} + \delta_{\text{LD}}^+) f_{+-} \frac{\Gamma_0^0(B^0 \rightarrow D^+ l \nu)}{\Gamma_0^0(B^+ \rightarrow D^0 l \nu)} + (\delta_{\text{SD}} + \delta_{\text{LD}}^0) f_{00} \frac{\Gamma_0^0(B^+ \rightarrow D^0 l \nu)}{\Gamma_0^0(B^0 \rightarrow D^+ l \nu)} \quad (63)$$

Assuming isospin symmetry at tree-level and averaging over both lepton modes, yields with $\frac{f_{+-}}{f_{00}} = 1.065(26)$ from [30] an overall correction of $\delta_{\text{total}} = 1.556(273)\%$ due to short- and long-distance next-to-leading order effects². This translates in a reduction of $-0.769(50)\%$ to the extracted value of $|V_{\text{cb}}|$.

Averaging the leptonic results yields for the $B^0 \rightarrow \pi^+ l \nu$ total decay rate an increase by $2.404(207)\%$, translating into a decrease of $-1.181(49)\%$ of extracted values of $|V_{\text{ub}}|$ from measurements. Similarly, the $B^+ \rightarrow \pi^0 l \nu$ total decay rate increases by $1.104(380)\%$, resulting into a decrease of $-0.548(92)\%$ of $|V_{\text{ub}}|$.

For $B^0 \rightarrow D_0^{*+} l \nu$ decays the total decay rate increases by $2.156(100)\%$, resulting in a decrease of $-1.061(24)\%$ of $|V_{\text{cb}}|$. Similarly the $B^+ \rightarrow D_0^{*0} l \nu$ total decay rate increases by $1.144(322)\%$, translating into a decrease of $-0.567(80)\%$ of $|V_{\text{cb}}|$. These results are summarized in Table 6.

5.2. Predictions for next-to-leading-order differential rates

In the following the normalized differential rates

$$\frac{1}{\Gamma} \frac{d\Gamma}{dp_l}, \quad \frac{1}{\Gamma} \frac{d\Gamma}{dp}, \quad \text{and} \quad \frac{1}{\Gamma} \frac{d\Gamma}{dk}, \quad (64)$$

for the tree-level and next-to-leading order decays are depicted, $\Gamma = \Gamma_0^0$ or $\Gamma = \Gamma_0^0 + \Gamma_1^0 + \Gamma_1^{\frac{1}{2}}$, respectively. The predictions are boosted into the rest frame of the $\Upsilon(4S) \rightarrow B \bar{B}$ decay. Figs. 7 and 8 depict the results for $B^0 \rightarrow D^+ e \nu(\gamma)$ and $B^0 \rightarrow D^+ \mu \nu(\gamma)$ decays. Figs. 9 and 10 depict correspondingly the $B^+ \rightarrow D^0 e \nu(\gamma)$ and $B^+ \rightarrow D^0 \mu \nu(\gamma)$ decays. The very massive D -meson only receives small corrections, whereas the electron three-momentum distributions are notably shifted towards smaller

²The uncertainty is propagated assuming a correlation of 100% between the matching and next-to-leading order uncertainties of each channel and a correlation of 100% between the isospin doublet. Further the uncertainties of f_{+-} and f_{00} are correlated by -100% .

three-momenta. The correction on the muon three-momentum distribution are smaller, due to its larger mass in comparison to the electron.

Figs. 11 and 12 depict the predictions for the $B^0 \rightarrow \pi^+ e \nu(\gamma)$ and $B^0 \rightarrow \pi^+ \mu \nu(\gamma)$ decay modes. The charged pion final state radiates notably and receives corrections in its shape. These are induced due to the radiative four-momentum transfer squared $t' = (p_B - p - k)^2$ dependency of the form factors.

The electron three-momentum distributions are shifted towards lower momenta, and the muon three-momentum distributions receive small corrections. Figs. 13 and 14 present the $B^+ \rightarrow \pi^0 e \nu(\gamma)$ and $B^+ \rightarrow \pi^0 \mu \nu(\gamma)$ decay modes. The uncharged pion receives negligible corrections from the radiative four-momentum transfer squared $t' = (p_B - p - k)^2$ due to the large mass of the B -meson, that heavily suppresses real next-to-leading order corrections.

Figs. 15 and 16 present the predictions for the $B^0 \rightarrow D_0^{*+} e \nu(\gamma)$ and $B^0 \rightarrow D_0^{*+} \mu \nu(\gamma)$ differential decay rates. The three-momentum of the D_0^{*+} , similarly as the D^+ case, only receives small corrections, whereas the electron three-momentum distribution is shifted to lower momenta, and the muon distribution receives small corrections. Similarly, Figs. 17 and 18 depict the predictions for the $B^+ \rightarrow D_0^{*0} e \nu(\gamma)$ and $B^+ \rightarrow D_0^{*0} \mu \nu(\gamma)$ differential decay rates.

The next-to-leading order differential rates $\frac{d\Gamma_0^0 + d\Gamma_0^1}{dp_l dp}$ and $\frac{d\Gamma_1^{\frac{1}{2}}}{dp_l dp dk}$ can be used to improve the measurements of the total decay rates of $B \rightarrow D l \nu$, $B \rightarrow \pi l \nu$, and $B \rightarrow D_0^* l \nu$ decays, and allow a more precise extraction of $|V_{ub}|$ and $|V_{cb}|$. The histograms of all shown Figures can be obtained at [29].

6. Conclusions

The long-distance next-to-leading order corrections for exclusive semileptonic B -meson decays in pseudoscalar and scalar final states was developed, and numerically evaluated for $B \rightarrow D l \nu$, $B \rightarrow \pi l \nu$, and $B \rightarrow D_0^* l \nu$ decays. The previously unknown long-distance enhancement to the total decay rate δ_{LD} was calculated for each mode, and the theoretical uncertainties were assessed: For the combined $B \rightarrow D l \nu$ total decay rate we find combining short- and long-distance effects a total correction of 1.556(96)% to the total decay rate. This results in the reduction of the extracted value of $|V_{cb}|$ of $-0.769(24)\%$. For the exclusive $B \rightarrow \pi^+ l \nu$ decays we find a correction of 2.404(207)% to the total rate due to next-to-leading order effects. This translates into a reduction of $|V_{ub}|$ by $-1.195(18)\%$ extracted from these decays.

In addition the next-to-leading order differential decay rates $\frac{1}{\Gamma} \frac{d\Gamma}{dp_l}$, $\frac{1}{\Gamma} \frac{d\Gamma}{dp}$, and $\frac{1}{\Gamma} \frac{d\Gamma}{dk}$ were presented for the scenario of the lepton either being an electron or a muon.

By providing the experimental community with these results and a next-to-leading order Monte Carlo generator, we close an important knowledge gap. The shown predictions for the correction of the total next-to-leading order decay rate, quantify the theoretical uncertainty of the extraction of the CKM matrix elements $|V_{ub}|$ and $|V_{cb}|$ from the studied pseudoscalar and scalar exclusive decays.

Acknowledgements

We thank Marek Schönherr for many great discussions and his help on the matter. Additional thanks goes to Dominik Stöckinger and Gino Isidori, who provided us with many useful comments, for which we are grateful. Last but not least we thank Troy Andre, Sasha Glazov, and Rick Kessler for the KLOR Monte Carlo generator.

	μ_0	δ_{SD}	δ_{LD}	δ_{total}
$B^0 \rightarrow D^+ e \nu$	$\frac{1}{2}m_b$	0.01752	0.00454(9)	0.02207(9)
	3.2 GeV/ c^2	0.01556	0.00560(9)	0.02116(9)
	m_b	0.01430	0.00619(9)	0.02049(9)
	5.2 GeV/ c^2	0.01331	0.00659(9)	0.01990(9)
	$2m_b$	0.01108	0.00727(9)	0.01835(9)
$B^0 \rightarrow D^+ \mu \nu$	$\frac{1}{2}m_b$	0.01752	0.00452(5)	0.02204(5)
	3.2 GeV/ c^2	0.01556	0.00558(5)	0.02115(5)
	m_b	0.01430	0.00617(5)	0.02048(5)
	5.2 GeV/ c^2	0.01331	0.00657(5)	0.01988(5)
	$2m_b$	0.01108	0.00727(5)	0.01835(5)
$B^+ \rightarrow D^0 e \nu$	$\frac{1}{2}m_b$	0.01752	-0.00366(8)	0.01386(8)
	3.2 GeV/ c^2	0.01556	-0.00394(8)	0.01163(8)
	m_b	0.01430	-0.00409(8)	0.01021(8)
	5.2 GeV/ c^2	0.01331	-0.00422(8)	0.00909(8)
	$2m_b$	0.01108	-0.00455(8)	0.00653(8)
$B^+ \rightarrow D^0 \mu \nu$	$\frac{1}{2}m_b$	0.01752	-0.00346(4)	0.01406(4)
	3.2 GeV/ c^2	0.01556	-0.00374(4)	0.01182(4)
	m_b	0.01430	-0.00390(4)	0.01041(4)
	5.2 GeV/ c^2	0.01331	-0.00402(4)	0.00929(4)
	$2m_b$	0.01108	-0.00436(4)	0.00672(4)

Table 2: The running of $1 + \delta_{\text{SD}} + \delta_{\text{LD}}$ as a function of μ_0 is shown. The uncertainty in the parenthesis is numerical.

	μ_0	δ_{SD}	δ_{LD}	δ_{total}
$B^0 \rightarrow \pi^+ e \nu$	$\frac{1}{2}m_b$	0.01752	0.00853(12)	0.02605(12)
	3.2 GeV/ c^2	0.01556	0.00926(12)	0.02482(12)
	m_b	0.01430	0.00975(12)	0.02405(12)
	5.2 GeV/ c^2	0.01331	0.01012(12)	0.02343(12)
	$2m_b$	0.01108	0.01083(12)	0.02192(12)
$B^0 \rightarrow \pi^+ \mu \nu$	$\frac{1}{2}m_b$	0.01752	0.00850(7)	0.02602(7)
	3.2 GeV/ c^2	0.01556	0.00923(7)	0.02480(7)
	m_b	0.01430	0.00973(7)	0.02404(7)
	5.2 GeV/ c^2	0.01331	0.01010(7)	0.02341(7)
	$2m_b$	0.01108	0.01083(7)	0.02191(7)
$B^+ \rightarrow \pi^0 e \nu$	$\frac{1}{2}m_b$	0.01752	-0.00269(9)	0.01483(9)
	3.2 GeV/ c^2	0.01556	-0.00313(9)	0.01243(9)
	m_b	0.01430	-0.00336(9)	0.01094(9)
	5.2 GeV/ c^2	0.01331	-0.00351(9)	0.00981(9)
	$2m_b$	0.01108	-0.00385(9)	0.00723(9)
$B^+ \rightarrow \pi^0 \mu \nu$	$\frac{1}{2}m_b$	0.01752	-0.00249(6)	0.01503(6)
	3.2 GeV/ c^2	0.01556	-0.00294(6)	0.01263(6)
	m_b	0.01430	-0.00316(6)	0.01114(6)
	5.2 GeV/ c^2	0.01331	-0.00331(6)	0.01000(6)
	$2m_b$	0.01108	-0.00365(6)	0.00744(6)

Table 3: See caption of Table 2.

	μ_0	δ_{SD}	δ_{LD}	δ_{total}
$B^0 \rightarrow D_0^{*+} e \nu$	$\frac{1}{2}m_b$	0.01752	0.00440(19)	0.02193(19)
	3.2 GeV/ c^2	0.01556	0.00593(19)	0.02149(19)
	m_b	0.01430	0.00685(19)	0.02115(19)
	5.2 GeV/ c^2	0.01331	0.00752(19)	0.02083(19)
	$2m_b$	0.01108	0.00886(19)	0.01994(19)
$B^0 \rightarrow D_0^{*+} \mu \nu$	$\frac{1}{2}m_b$	0.01752	0.00519(5)	0.02271(5)
	3.2 GeV/ c^2	0.01556	0.00673(5)	0.02229(5)
	m_b	0.01430	0.00766(5)	0.02196(5)
	5.2 GeV/ c^2	0.01331	0.00833(5)	0.02164(5)
	$2m_b$	0.01108	0.00968(5)	0.02076(5)
$B^+ \rightarrow D_0^{*0} e \nu$	$\frac{1}{2}m_b$	0.01752	-0.00297(19)	0.01455(19)
	3.2 GeV/ c^2	0.01556	-0.00305(19)	0.01285(19)
	m_b	0.01430	-0.00304(19)	0.01126(19)
	5.2 GeV/ c^2	0.01331	-0.00303(19)	0.01028(19)
	$2m_b$	0.01108	-0.00298(19)	0.00810(19)
$B^+ \rightarrow D_0^{*0} \mu \nu$	$\frac{1}{2}m_b$	0.01752	-0.00261(4)	0.01491(4)
	3.2 GeV/ c^2	0.01556	-0.00268(4)	0.01321(4)
	m_b	0.01430	-0.00268(4)	0.01163(4)
	5.2 GeV/ c^2	0.01331	-0.00266(4)	0.01065(4)
	$2m_b$	0.01108	-0.00260(4)	0.00848(4)

Table 4: See caption of Table 2.

	$1 + \delta_{\text{SD}} + \delta_{\text{LD}}$	$\sqrt{1 + \delta_{\text{SD}} + \delta_{\text{LD}}}$
$B^0 \rightarrow D^+ e \nu$	1.02049(9 ± 15 ± 186)	1.01019(2 ± 4 ± 45)
$B^0 \rightarrow D^+ \mu \nu$	1.02048(5 ± 15 ± 185)	1.01019(1 ± 4 ± 45)
$B^+ \rightarrow D^0 e \nu$	1.01021(8 ± 7 ± 367)	1.00509(2 ± 2 ± 91)
$B^+ \rightarrow D^0 \mu \nu$	1.01073(4 ± 8 ± 367)	1.00519(1 ± 2 ± 91)
	$1 + \delta_{\text{SD}} + \delta_{\text{LD}}$	$\sqrt{1 + \delta_{\text{SD}} + \delta_{\text{LD}}}$
$B^0 \rightarrow \pi^+ e \nu$	1.02405(12 ± 18 ± 207)	1.01195(3 ± 4 ± 51)
$B^0 \rightarrow \pi^+ \mu \nu$	1.02404(7 ± 18 ± 206)	1.01195(2 ± 4 ± 50)
$B^+ \rightarrow \pi^0 e \nu$	1.01094(9 ± 8 ± 380)	1.00546(2 ± 2 ± 94)
$B^+ \rightarrow \pi^0 \mu \nu$	1.01114(6 ± 8 ± 380)	1.00556(1 ± 2 ± 94)
	$1 + \delta_{\text{SD}} + \delta_{\text{LD}}$	$\sqrt{1 + \delta_{\text{SD}} + \delta_{\text{LD}}}$
$B^0 \rightarrow D_0^{*+} e \nu$	1.02115(19 ± 15 ± 99)	1.01052(5 ± 4 ± 24)
$B^0 \rightarrow D_0^{*+} \mu \nu$	1.02196(5 ± 16 ± 98)	1.01092(1 ± 4 ± 24)
$B^+ \rightarrow D_0^{*0} e \nu$	1.01126(19 ± 8 ± 322)	1.00561(5 ± 2 ± 80)
$B^+ \rightarrow D_0^{*0} \mu \nu$	1.01163(4 ± 8 ± 322)	1.00580(1 ± 2 ± 80)

Table 5: Integration results for $t \neq t'$ expressions gained via Ward identity: The predictions for the summed next-to-leading corrections are listed. The uncertainty in the parenthesis are numerical, next-to-next-to-leading order, and due to the matching of the short-distance and long-distance picture.

	$1 + \delta_{\text{SD}} + \delta_{\text{LD}}$	$\sqrt{1 + \delta_{\text{SD}} + \delta_{\text{LD}}}$
$B^0 \rightarrow D^+ l \nu$	1.02048(186)	1.01019(45)
$B^+ \rightarrow D^0 l \nu$	1.01031(367)	1.00514(91)
$B \rightarrow D l \nu$	1.01556(273)	1.00775(69)
	$1 + \delta_{\text{SD}} + \delta_{\text{LD}}$	$\sqrt{1 + \delta_{\text{SD}} + \delta_{\text{LD}}}$
$B^0 \rightarrow \pi^+ l \nu$	1.02404(207)	1.01195(51)
$B^+ \rightarrow \pi^0 l \nu$	1.01104(380)	1.00551(94)
	$1 + \delta_{\text{SD}} + \delta_{\text{LD}}$	$\sqrt{1 + \delta_{\text{SD}} + \delta_{\text{LD}}}$
$B^0 \rightarrow D_0^{*+} l \nu$	1.02156(100)	1.01072(25)
$B^+ \rightarrow D_0^{*0} l \nu$	1.01144(322)	1.00571(80)

Table 6: Averaged integration results for $t \neq t'$ expressions gained via Ward identity: The uncertainty in the parenthesis is the sum of numerical, next-to-next-to-leading order, and due to the matching of the short-distance and long-distance picture uncertainties.

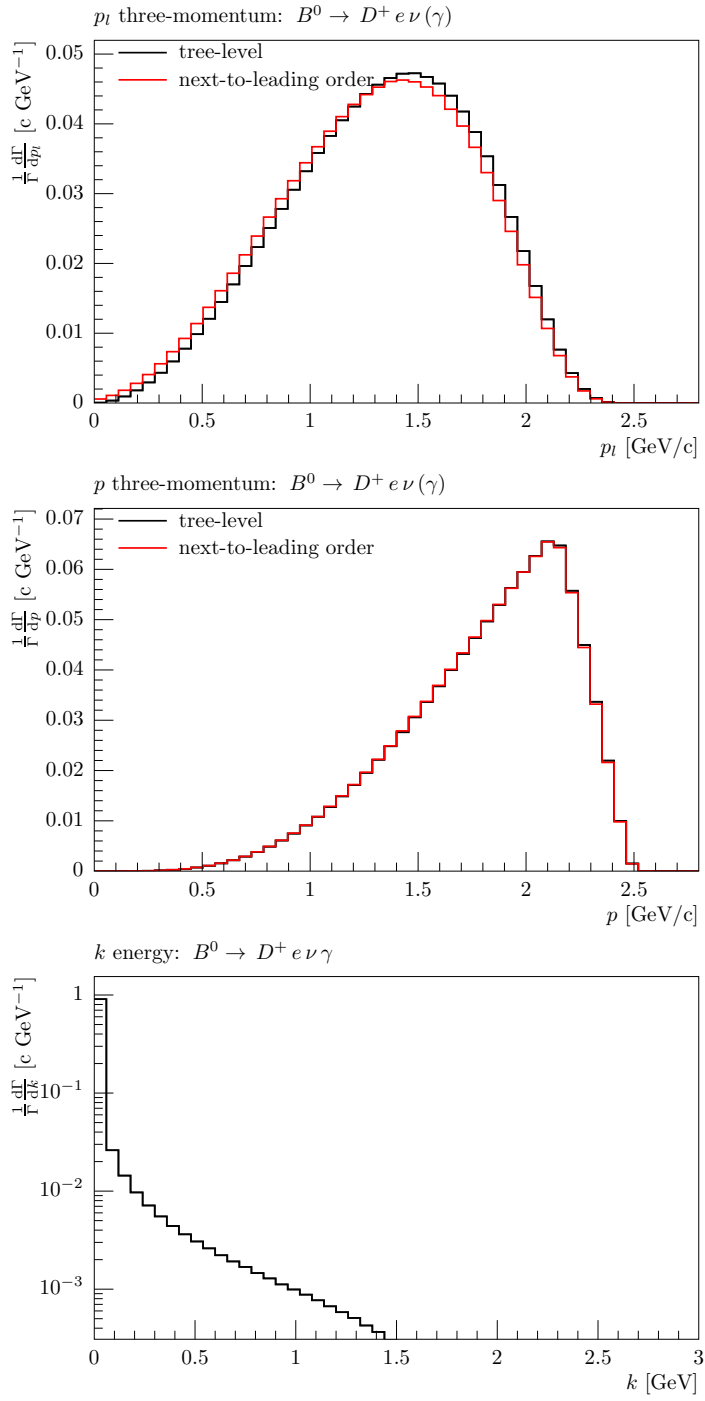


Figure 7: $B^0 \rightarrow D^+ e \nu$: The predicted lepton and D three-momentum magnitudes, p_l and p , for tree-level and next-to-leading order and the logarithmic photon energy k distribution are shown.

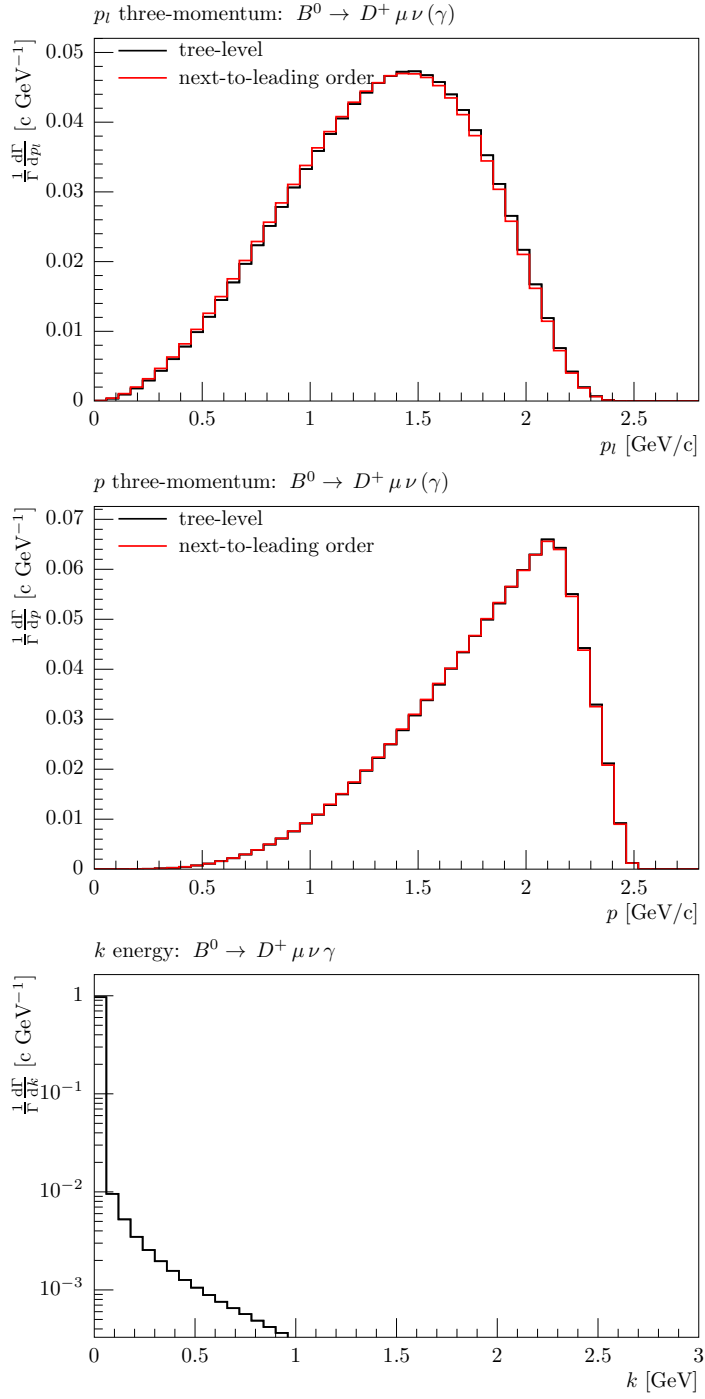


Figure 8: $B^0 \rightarrow D^+ \mu \nu$: See caption of Fig. 7.

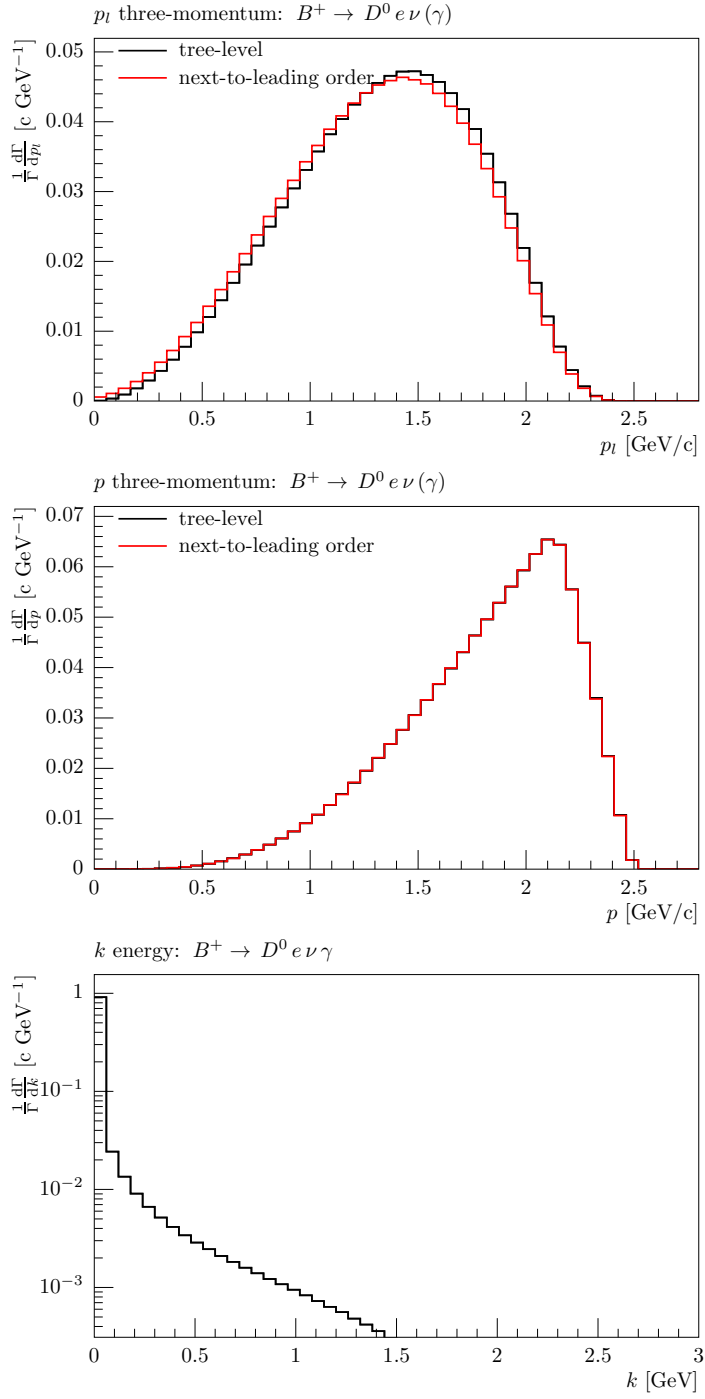


Figure 9: $B^+ \rightarrow D^0 e \nu$: See caption of Fig. 7.

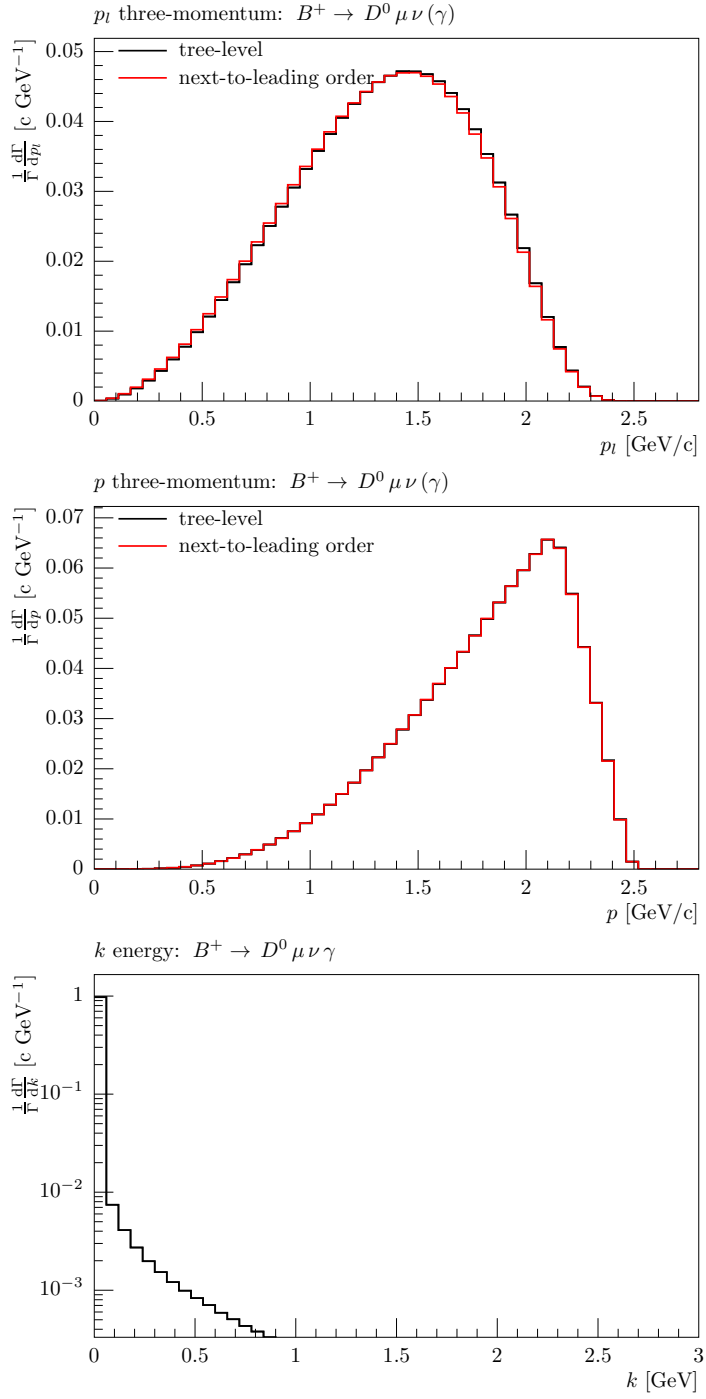


Figure 10: $B^+ \rightarrow D^0 \mu \nu$: See caption of Fig. 7.

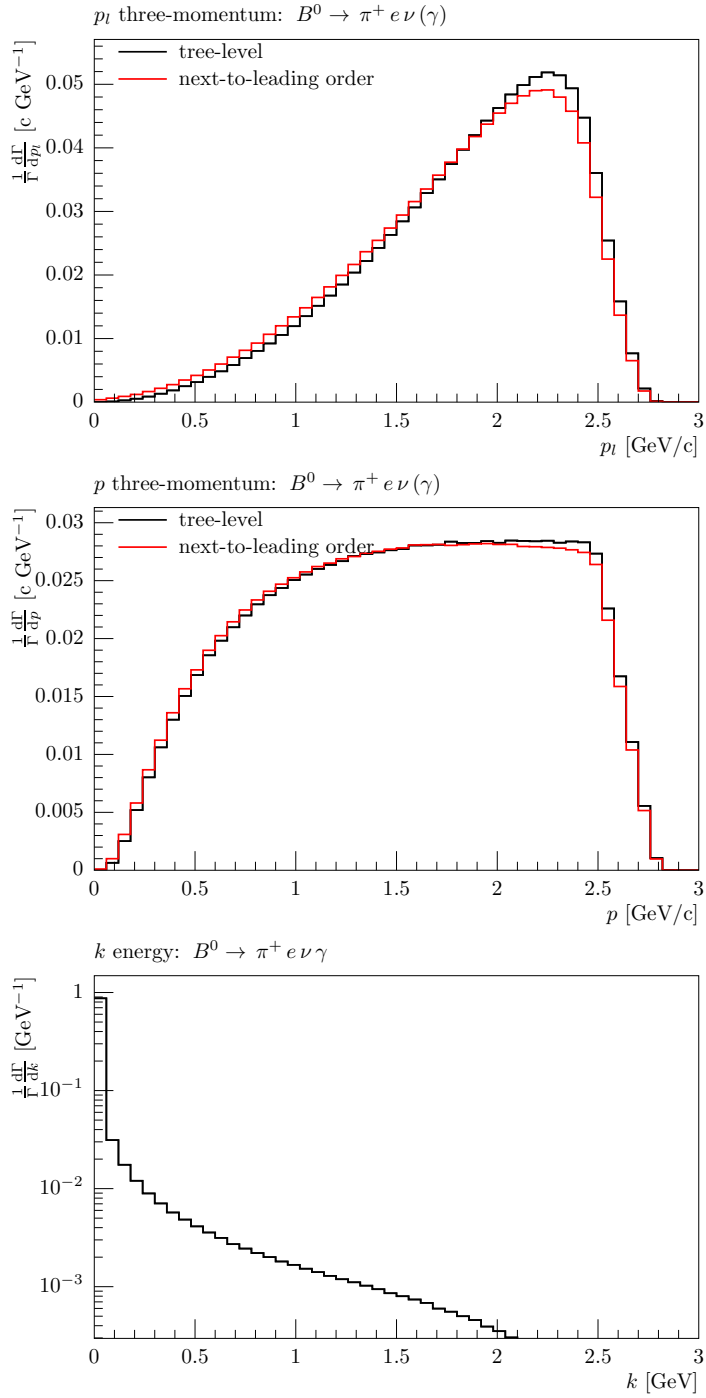


Figure 11: $B^0 \rightarrow \pi^+ e \nu(\gamma)$: The predicted lepton and π three-momentum magnitudes, p_l and p , for tree-level and next-to-leading order and the logarithmic photon energy k distribution are shown.

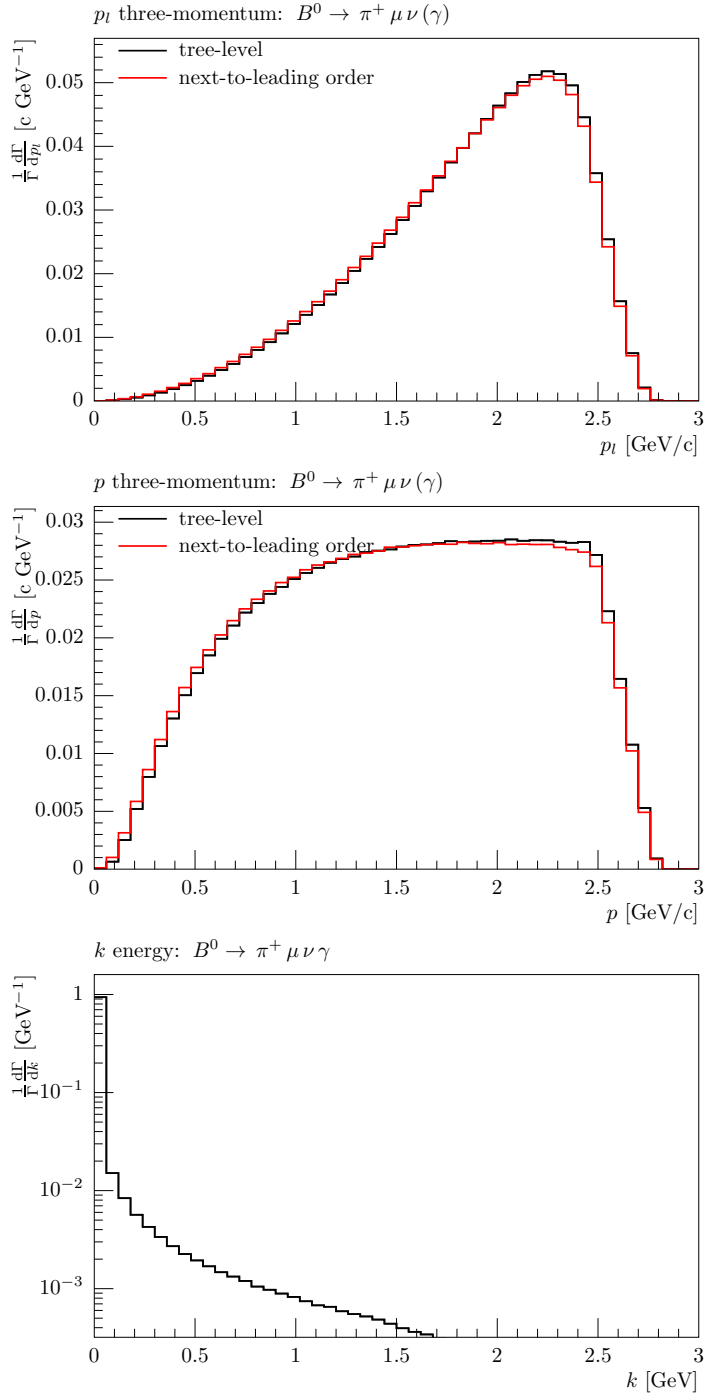


Figure 12: $B^0 \rightarrow \pi^+ \mu \nu (\gamma)$: See caption of Fig. 11.

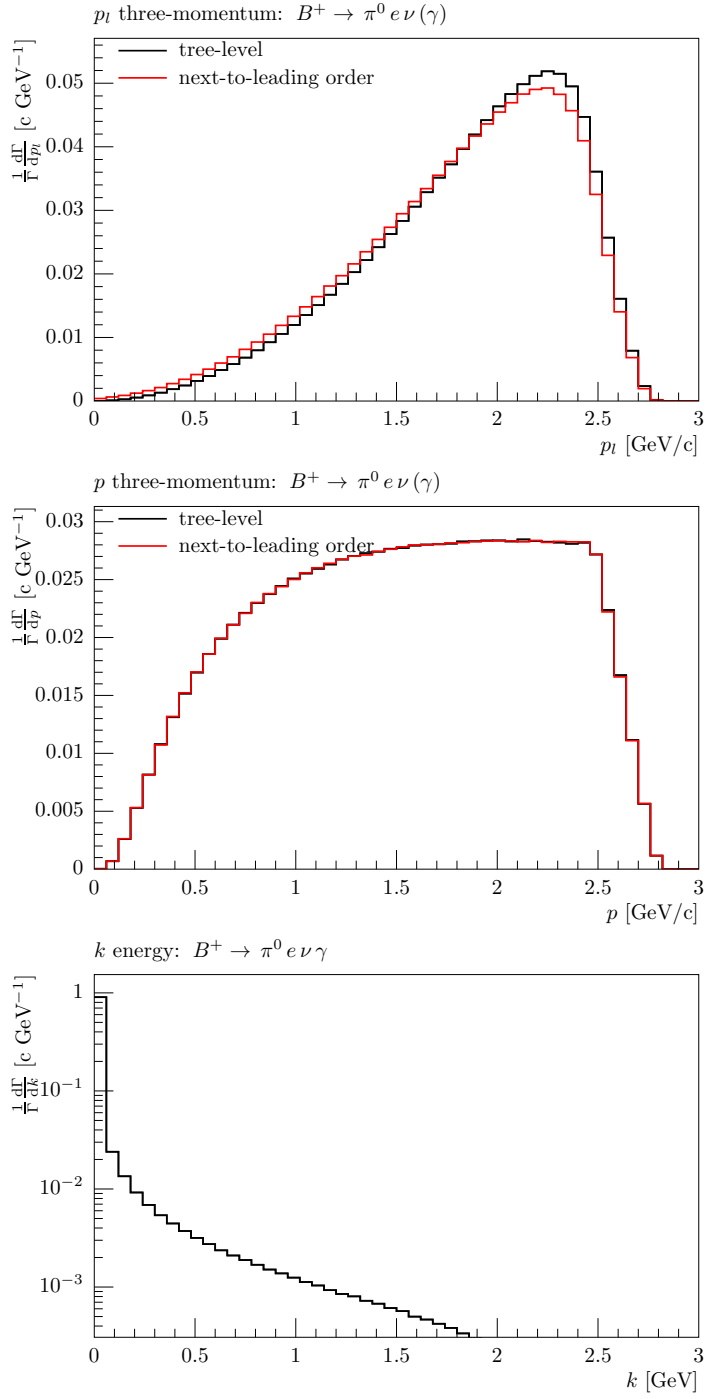


Figure 13: $B^+ \rightarrow \pi^0 e \nu(\gamma)$: See caption of Fig. 11.

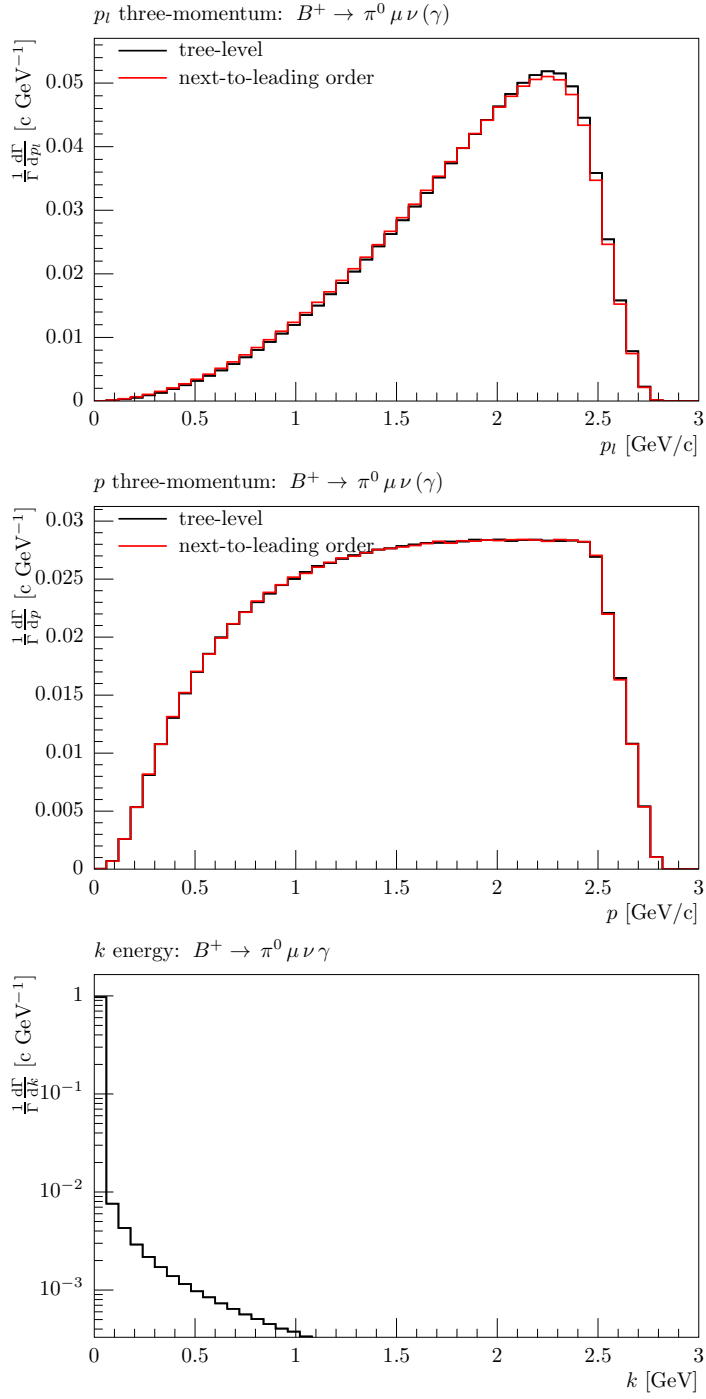


Figure 14: $B^+ \rightarrow \pi^0 \mu \nu (\gamma)$: See caption of Fig. 11.

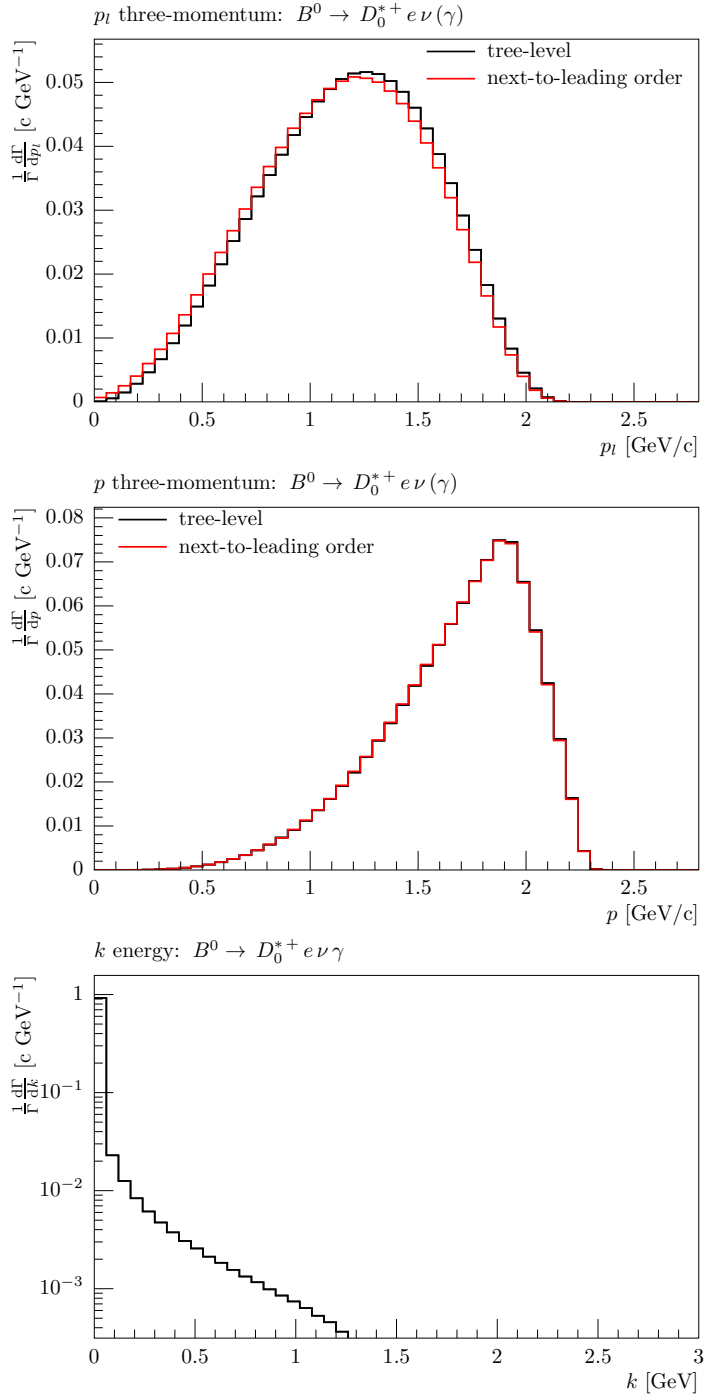


Figure 15: $B^0 \rightarrow D_0^{*+} l \nu (\gamma)$: The predicted lepton and D_0^* three-momentum magnitudes, p_l and p , for tree-level and next-to-leading order and the logarithmic photon energy k distribution are shown.

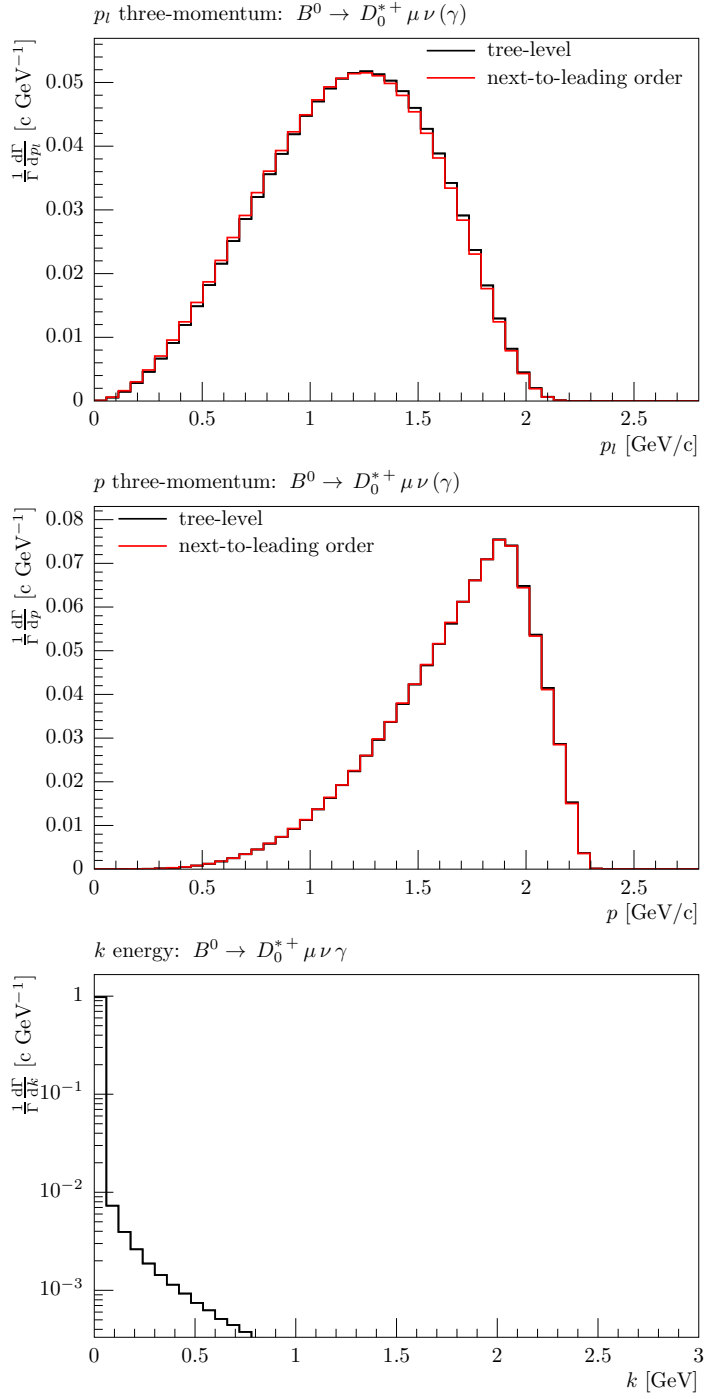


Figure 16: $B^0 \rightarrow D_0^{*+} \mu \nu (\gamma)$: See caption of Fig. 15.

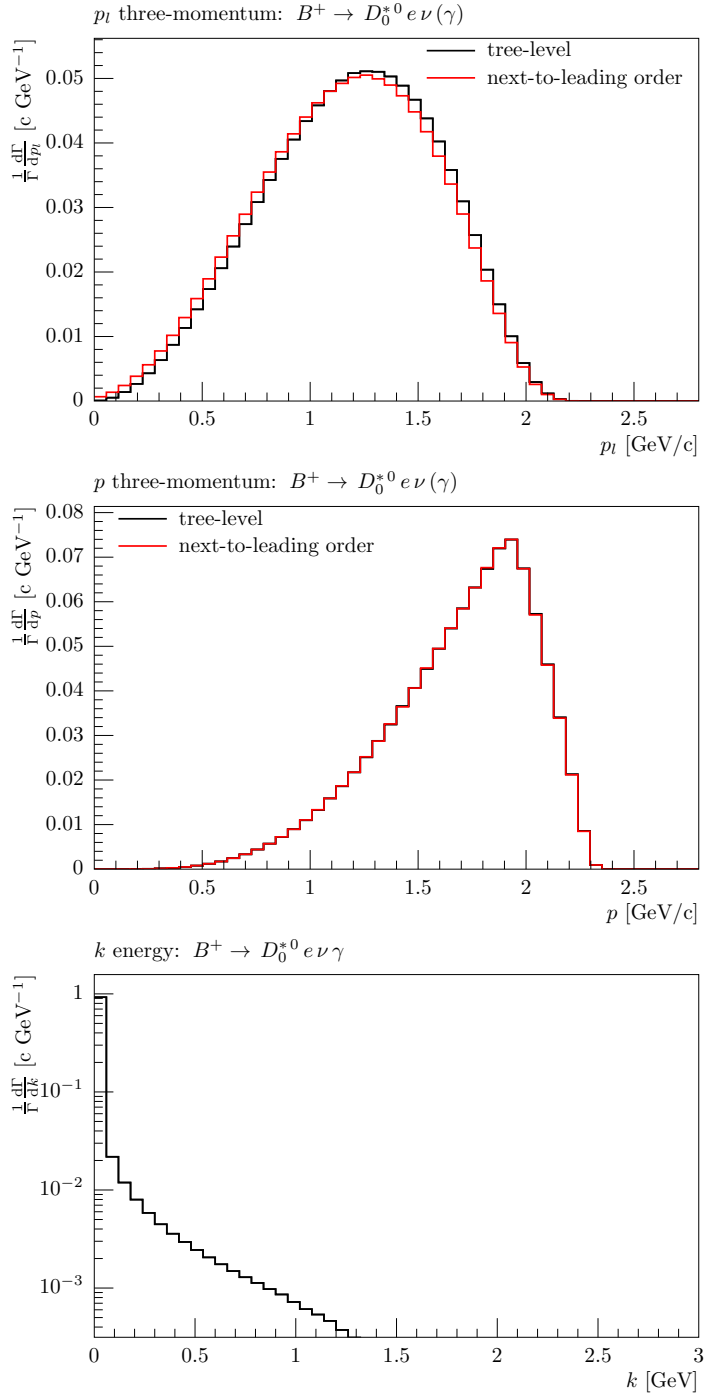


Figure 17: $B^+ \rightarrow D_0^{*0} e \nu(\gamma)$: See caption of Fig. 15.

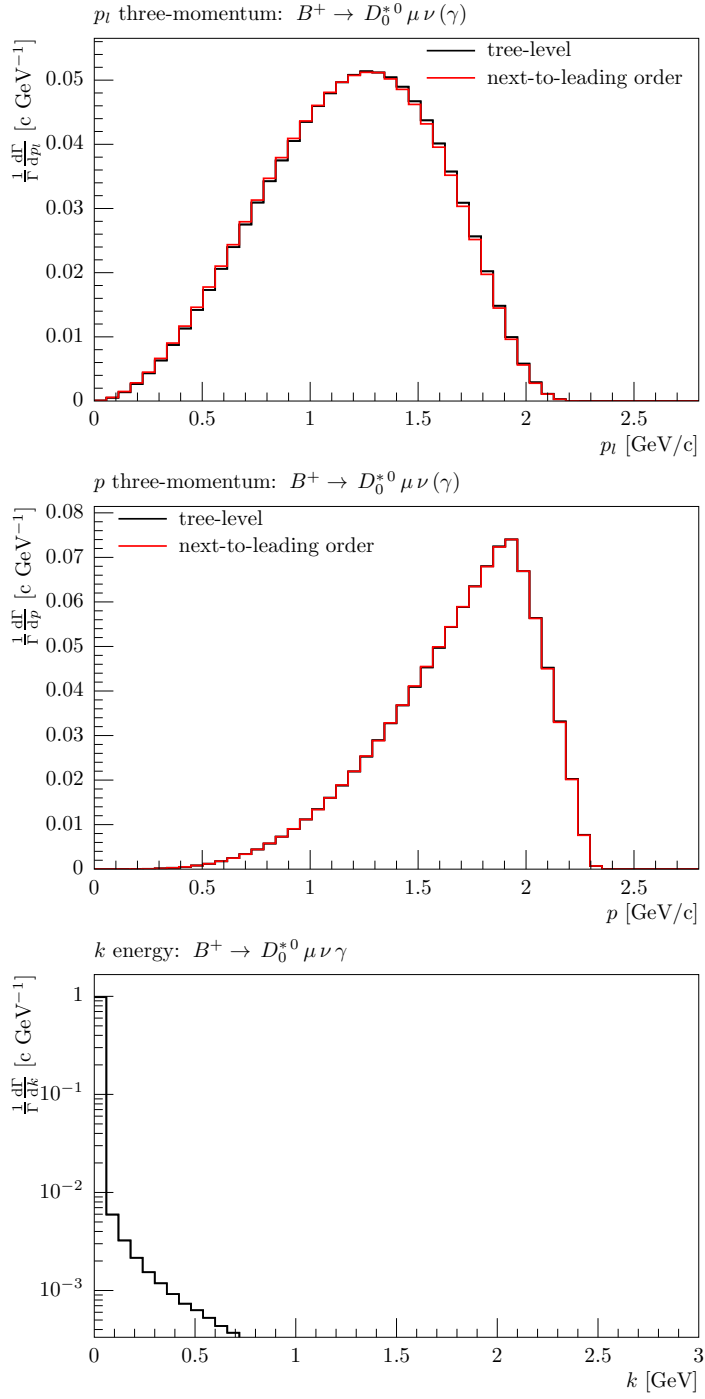


Figure 18: $B^+ \rightarrow D_0^{*0} \mu \nu (\gamma)$: See caption of Fig. 15.

A. Form factor models of exclusive semileptonic B -meson decays reviewed.

A.1. Form factors for $B \rightarrow D l \nu$

Considering the heavy quark sector of the standard model Lagrangian in the limit of infinitely massive quarks yields interesting simplifications: The arising effective field theory is known as heavy quark effective theory [33] and predicts the expansion of the hadronic current for exclusive $B \rightarrow D l \nu$ decays as a function of the four-velocity transfer $w = v_B \cdot v_D$, where v_B and v_D are the four velocities of the B - or D -meson, respectively. The relevant vector current is

$$\langle D | V^\mu | B \rangle = \sqrt{m_B m_D} \left(h_+(w) (v_B + v_D)^\mu + h_-(w) (v_B - v_D)^\mu \right), \quad (65)$$

with the heavy quark form factors

$$h_+(w) = \mathcal{G}(1) \times \left[1 - 8\rho_D^2 z + (51\rho_D^2 - 10)z^2 - (252\rho_D^2 - 84)z^3 \right], \quad (66)$$

$$h_-(w) = 0, \quad (67)$$

where $z = \frac{\sqrt{w+1}-\sqrt{2}}{\sqrt{w+1}+\sqrt{2}}$. The expansion depends on ρ_D^2 and $\mathcal{G}(1)$, which are the form factor slope and the normalization at $w = 1$, respectively. The numerical value of the slope used in this analysis is listed in Table 7.

Parameter	Value
ρ_D^2	1.19

Table 7: Used averaged slope taken from [34].

A.2. Form factors for $B \rightarrow \pi l \nu$

Extrapolating results from lattice QCD calculations and light-cone sum rules the form factors of exclusive $B \rightarrow \pi l \nu$ can be parametrized as a function of the four-momentum transfer squared t . The relevant vector current is [35]

$$\langle \pi | V^\mu | B \rangle = \left((p_B + p_\pi)^\mu - \frac{m_B^2 - m_\pi^2}{t} (p_B - p_\pi)^\mu \right) f_+(t) + \left(\frac{m_B^2 - m_\pi^2}{t} (p_B - p_\pi)^\mu \right) f_0(t), \quad (68)$$

with form factors parametrized as

$$f_+(t) = \frac{r_{f_{+1}}}{1 - \frac{t}{m_{f_{+1}}^2}} + \frac{r_{f_{+2}}}{1 - \frac{t}{m_{f_{+2}}^2}}, \quad (69)$$

$$f_0(t) = \frac{r_{f_0}}{1 - \frac{t}{m_{f_0}^2}}, \quad (70)$$

with the normalizations $r_{f_{+1}}, r_{f_{+2}}$, and r_{f_0} , and the pole masses $m_{f_{+1}}, m_{f_{+2}}$, and m_{f_0} . The values used in this paper are stated in Table 8. The q^μ proportional form factor $f_-(t)$ can be written as

$$f_-(t) = \frac{m_B^2 - m_\pi^2}{t} \left(f_0(t) - f_+(t) \right) = \frac{m_B^2 - m_\pi^2}{t} \left(\frac{r_{f_0}}{1 - \frac{t}{m_{f_0}^2}} - \frac{r_{f_{+1}}}{1 - \frac{t}{m_{f_{+1}}^2}} - \frac{r_{f_{+2}}}{1 - \frac{t}{m_{f_{+2}}^2}} \right), \quad (71)$$

Parameter		Value
$r_{f_{+1}}$		0.744
$r_{f_{+2}}$		-0.486
$m_{f_{+1}}^2$	GeV ² /c ⁴	28.40
$m_{f_{+2}}^2$	GeV ² /c ⁴	40.73
r_{f_0}		0.258
$m_{f_0}^2$	GeV ² /c ⁴	33.81

Table 8: Form factor slopes and pole masses taken from [35].

A.3. Form factors for $B \rightarrow D_0^* l \nu$

Heavy quark effective theory can be used to extract differential and total rates for other charmed resonances in an approximative manor, as done in [36, 37] for $B \rightarrow D_0^* l \nu$ decays. Since the D_0^* is a scalar particle, the hadronic vector current vanishes and only axial contributions survive. The relevant hadronic contribution is given by

$$\langle D_0^* | A^\mu | B \rangle = \sqrt{m_B m_{D_0^*}} \left(g_+(w) (v_B + v_{D_0^*})^\mu + g_-(w) (v_B - v_{D_0^*})^\mu \right). \quad (72)$$

with the form factors g_\pm . They are parametrized by

$$\begin{aligned} g_+(w) &= \epsilon_c \left[2(w-1)\zeta_1(w) - 3\zeta(w) \frac{w\bar{\Lambda}^* - \bar{\Lambda}}{w+1} \right] - \epsilon_b \left[\frac{\bar{\Lambda}^*(2w+1) - \bar{\Lambda}(w+2)}{w+1} \zeta(w) - 2(w-1)\zeta_1(w) \right], \\ g_-(w) &= \zeta(w), \end{aligned} \quad (73)$$

where

$$\zeta(w) = \frac{w+1}{\sqrt{3}} \tau(w). \quad (74)$$

with $\tau(w)$ the leading Isgur-wise function [38]. This can be simplified into

$$\zeta(w) = \zeta(1) \times [1 + \zeta'(w-1)]. \quad (75)$$

where ζ' denotes the form factor slope. The value of ζ_1 depends on the phase-space region, but its exact value only leads to small corrections. As a consequence its contributions can either be neglected or approximatively taken into account. The latter is done by setting

$$\zeta_1 = \bar{\Lambda} \zeta(w). \quad (76)$$

The numerical values of the remaining slopes and pole masses are stated in Table 9.

Parameter		Value
ϵ_b	c GeV ⁻¹	0.1042
ϵ_c	c GeV ⁻¹	0.3571
$\bar{\Lambda}$	GeV/c ²	0.4
$\bar{\Lambda}^*$	GeV/c ²	0.75
ζ'		-1.0

Table 9: Form factor slopes and pole masses taken from [36].

B. Form factor model dependent terms for $t \neq t'$

B.1. $Z_{f_{\pm}}(t, k)$ from $B \rightarrow D l \nu$ form factors

To extract $Z_{f_{\pm}}(t, k)$ we first need to translate the impact of the photon four-momentum k into the velocity transfer w (see Sec. A.1). It is

$$w' = w + \frac{k(p_B - p_X)}{m_B m_X} = w + k'. \quad (77)$$

This yields for the ratio z

$$z' = \frac{\sqrt{w'+1} - \sqrt{2}}{\sqrt{w'+1} + \sqrt{2}} = z + \frac{2\sqrt{2}(\sqrt{w+1+k'} - \sqrt{w+1})}{(\sqrt{w+1+k'} + \sqrt{2})(\sqrt{w+1} + \sqrt{2})}, \quad (78)$$

$$z'^2 = \left(\frac{\sqrt{w'+1} - \sqrt{2}}{\sqrt{w'+1} + \sqrt{2}} \right)^2 = z^2 + z \frac{4\sqrt{2}(\sqrt{w+1+k'} - \sqrt{w+1})}{(\sqrt{w+1+k'} + \sqrt{2})(\sqrt{w+1} + \sqrt{2})} + \frac{8(\sqrt{w+1+k'} - \sqrt{w+1})^2}{(\sqrt{w+1+k'} + \sqrt{2})^2(\sqrt{w+1} + \sqrt{2})^2}, \quad (79)$$

$$z'^3 = \left(\frac{\sqrt{w'+1} - \sqrt{2}}{\sqrt{w'+1} + \sqrt{2}} \right)^3 = z^3 + z \frac{24\sqrt{2}(\sqrt{w+1+k'} - \sqrt{w+1})^2}{(\sqrt{w+1+k'} + \sqrt{2})^2(\sqrt{w+1} + \sqrt{2})^2} + z^2 \frac{6\sqrt{2}(\sqrt{w+1+k'} - \sqrt{w+1})}{(\sqrt{w+1+k'} + \sqrt{2})(\sqrt{w+1} + \sqrt{2})} + \frac{16\sqrt{2}(\sqrt{w+1+k'} - \sqrt{w+1})^3}{(\sqrt{w+1+k'} + \sqrt{2})^3(\sqrt{w+1} + \sqrt{2})^3}, \quad (80)$$

With this result we find for the heavy quark form factor

$$h_+(w') = \mathcal{G}(1) \times \left[1 - 8\rho_D^2 z' + (51\rho_D^2 - 10) z'^2 - (252\rho_D^2 - 84) z'^3 \right], \quad (81)$$

$$\begin{aligned} &= \mathcal{G}(1) \times \left[1 - 8\rho_D^2 z - 8\rho_D^2 \frac{2\sqrt{2}(\sqrt{w+1+k'} - \sqrt{w+1})}{(\sqrt{w+1+k'} + \sqrt{2})(\sqrt{w+1} + \sqrt{2})} \right. \\ &\quad + (51\rho_D^2 - 10) z^2 + (51\rho_D^2 - 10) z \frac{4\sqrt{2}(\sqrt{w+1+k'} - \sqrt{w+1})}{(\sqrt{w+1+k'} + \sqrt{2})(\sqrt{w+1} + \sqrt{2})} \\ &\quad + (51\rho_D^2 - 10) \frac{8(\sqrt{w+1+k'} - \sqrt{w+1})^2}{(\sqrt{w+1+k'} + \sqrt{2})^2(\sqrt{w+1} + \sqrt{2})^2} \\ &\quad - (252\rho_D^2 - 84) z^3 - (252\rho_D^2 - 84) z \frac{24\sqrt{2}(\sqrt{w+1+k'} - \sqrt{w+1})^2}{(\sqrt{w+1+k'} + \sqrt{2})^2(\sqrt{w+1} + \sqrt{2})^2} \\ &\quad - (252\rho_D^2 - 84) z^2 \frac{6\sqrt{2}(\sqrt{w+1+k'} - \sqrt{w+1})}{(\sqrt{w+1+k'} + \sqrt{2})(\sqrt{w+1} + \sqrt{2})} \\ &\quad \left. - (252\rho_D^2 - 84) \frac{16\sqrt{2}(\sqrt{w+1+k'} - \sqrt{w+1})^3}{(\sqrt{w+1+k'} + \sqrt{2})^3(\sqrt{w+1} + \sqrt{2})^3} \right], \quad (82) \end{aligned}$$

$$= h_+(w) + Z_{h_+}(w, k), \quad (83)$$

which translates into

$$f_+(t') = f_+(t) + \frac{1}{2}\sqrt{m_B m_D} \left(\frac{1}{m_B} + \frac{1}{m_D} \right) Z_{h_+}(w, k) = f_+(t) + Z_{f_+}(t, k), \quad (84)$$

$$f_-(t') = f_-(t) + \frac{1}{2}\sqrt{m_B m_D} \left(\frac{1}{m_B} - \frac{1}{m_D} \right) Z_{h_+}(w, k) = f_-(t) + Z_{f_-}(t, k). \quad (85)$$

To invert the Ward-transformation the correction factors $Z_{f\pm}(t, k)$ has to be factorizable in k . Expanding the relevant term in Eqn. (83)

$$Z_w^n(w, k) = \left(\frac{(\sqrt{w+1+k'} - \sqrt{w+1})}{(\sqrt{w+1+k'+\sqrt{2}})(\sqrt{w+1+\sqrt{2}})} \right)^n, \quad (86)$$

yields

$$Z_w^1(w, k) = k_a \frac{(p_B - p_X)^a}{m_B m_X} \left(\frac{1}{2(\sqrt{2} + \sqrt{w+1})^2 \sqrt{w+1}} + \frac{(-3\sqrt{w+1} - \sqrt{2})k'}{8(\sqrt{w+1} + \sqrt{2})^3 (w+1)^{3/2}} + \frac{2 + 4\sqrt{2}\sqrt{w+1} + 5(w+1)k'^2}{16(\sqrt{w+1} + \sqrt{2})^4 (w+1)^{5/2}} + \mathcal{O}(k'^3) \right), \quad (87)$$

$$= k_a Z_w^{1a}(w, k), \quad (88)$$

$$Z_w^2(w, k) = k_a \frac{(p_B - p_X)^a}{m_B m_X} \left(\frac{k'}{4(\sqrt{2} + \sqrt{w+1})^4 (w+1)} + \frac{(-3\sqrt{w+1} - \sqrt{2})k'^2}{8(\sqrt{w+1} + \sqrt{2})^5 (w+1)^2} + \mathcal{O}(k'^3) \right) \quad (89)$$

$$= k_a Z_w^{2a}(w, k), \quad (90)$$

$$Z_w^3(w, k) = k_a \frac{(p_B - p_X)^a}{m_B m_X} \left(\frac{k'^2}{8(\sqrt{2} + \sqrt{w+1})^6 (w+1)^{3/2}} + \mathcal{O}(k'^3) \right), \quad (91)$$

$$= k_a Z_w^{3a}(w, k). \quad (92)$$

Eqn. (83) expands as

$$Z_{h_+}(w, k) = \mathcal{G}(1) \times \left[-16\sqrt{2}\rho_D^2 Z_w^1(w, k) + 4\sqrt{2}(51\rho_D^2 - 10) z Z_w^1(w, k) + 8(51\rho_D^2 - 10) Z_w^2(w, k) - 24\sqrt{2}(252\rho_D^2 - 84) z Z_w^2(w, k) - 6\sqrt{2}(252\rho_D^2 - 84) z^2 Z_w^1(w, k) - 16\sqrt{2}(252\rho_D^2 - 84) Z_w^3(w, k) \right], \quad (93)$$

$$= \mathcal{G}(1) \times k_a \left[-16\sqrt{2}\rho_D^2 Z_w^{1a}(w, k) + 4\sqrt{2}(51\rho_D^2 - 10) z Z_w^{1a}(w, k) + 8(51\rho_D^2 - 10) Z_w^{2a}(w, k) - 24\sqrt{2}(252\rho_D^2 - 84) z Z_w^{2a}(w, k) - 6\sqrt{2}(252\rho_D^2 - 84) z^2 Z_w^{1a}(w, k) - 16\sqrt{2}(252\rho_D^2 - 84) Z_w^{3a}(w, k) \right], \quad (94)$$

$$= k_a Z_{h_+}^a(w, k), \quad (95)$$

and one identifies

$$Z_{f_+}(t, k) = \frac{1}{2}\sqrt{m_B m_D} \left(\frac{1}{m_B} + \frac{1}{m_D} \right) k_a Z_{h_+}^a(w, k), \quad (96)$$

$$= k_a Z_{f_+}^a(t, k),$$

$$Z_{f_-}(t, k) = \frac{1}{2}\sqrt{m_B m_D} \left(\frac{1}{m_B} - \frac{1}{m_D} \right) k_a Z_{h_+}^a(w, k), \quad (97)$$

$$= k_a Z_{f_-}^a(t, k).$$

B.2. $Z_{f\pm}(t, k)$ from $B \rightarrow \pi l \nu$ form factors

The photon four-momentum k changes the momentum transfer squared as

$$t' = (p_B - p_\pi - k)^2 = t - 2k(p_B - p_\pi) = t + k'. \quad (98)$$

The $B \rightarrow \pi l \nu$ form factors change according to (see Sec. A.2)

$$\begin{aligned} f_+(t') &= \frac{r_{f_{+1}}}{1 - \frac{t'}{m_{f_{+1}}^2}} + \frac{r_{f_{+2}}}{1 - \frac{t'}{m_{f_{+2}}^2}}, \\ &= f_+(t) + k_\alpha Z_{f_{+}}^\alpha(t, k), \end{aligned} \quad (99)$$

$$\begin{aligned} f_0(t') &= \frac{r_{f_0}}{1 - \frac{t'}{m_{f_0}^2}}, \\ &= f_0(t) + k_\alpha Z_{f_0}^\alpha(t, k) \end{aligned} \quad (100)$$

Expanding about $k = 0$ in case of $t - m_{f_{+1}} < k'$ and $t - m_{f_{+2}} < k'$ yields

$$k_\alpha Z_{f_{+}}^\alpha(t, k) = \left((k)_\alpha (p_B - p_\pi)^\alpha \right) \sum_{n=1}^m \sum_{i=1}^2 (-2)^n e_n^i \left(k \cdot (p_B - p_\pi) \right)^{n-1}, \quad (101)$$

$$k_\alpha Z_{f_0}^\alpha(t, k) = \left((k)_\alpha (p_B - p_\pi)^\alpha \right) \sum_{n=1}^m (-2)^n f_n \left(k \cdot (p_B - p_\pi) \right)^{n-1}, \quad (102)$$

with parameters

$$e_n^1 = \left(\frac{r_{f_{+1}}}{m_{f_{+1}}^{2n} \left(1 - \frac{t}{m_{f_{+1}}^2} \right)^{n+1}} \right), \quad (103)$$

$$e_n^2 = \left(\frac{r_{f_{+2}}}{m_{f_{+2}}^{2n} \left(1 - \frac{t}{m_{f_{+2}}^2} \right)^{n+1}} \right), \quad (104)$$

$$f_n = \frac{m_{f_0}^2 r_{f_0}}{(m_{f_0}^2 - t)^{n+1}}. \quad (105)$$

In the rare case of $t - m_{f_{+1}} > k'$ or $t - m_{f_{+2}} > k'$ we use

$$\hat{e}_1^1 = \left(\frac{2}{k'} \frac{r_{f_{+1}}}{1 - \frac{t}{m_{f_{+1}}^2}} - \frac{2}{k'} \frac{r_{f_{+1}}}{1 - \frac{t+k'}{m_{f_{+1}}^2}} \right), \quad (106)$$

$$\hat{e}_1^2 = \left(\frac{2}{k'} \frac{r_{f_{+2}}}{1 - \frac{t}{m_{f_{+2}}^2}} - \frac{2}{k'} \frac{r_{f_{+2}}}{1 - \frac{t+k'}{m_{f_{+2}}^2}} \right), \quad (107)$$

with $\hat{e}_i^n = 0$ for $n > 1$ and $i = 1, 2$. In the phase-space region of hard radiation from the final state pion, s.t. it almost comes to rest in the B -meson rest frame, the convergence behavior of Eqns. (101) and is very slow and we make use of

$$k_\alpha Z_{f_\pm}^\alpha(t, k) = k' \left(\frac{f_\pm(t')}{k'} - \frac{f_\pm(t)}{k'} \right). \quad (108)$$

B.3. $Z_{f\pm}(t, k)$ from $B \rightarrow D_0^* l \nu$ form factors

With $w' = w + k'$ according to Eqn. (77) the $B \rightarrow D_0^* l \nu$ form factors (see Sec. A.3) can be expanded as

$$\begin{aligned}
g_+(w') &= g_+(w) + \zeta(1) \times \left[\frac{\epsilon_b \left((1 - \zeta' + w(4 - 2\zeta' + 2w + 5\zeta'w + 4\zeta'w^2))\bar{\Lambda} - (1 + 2w(2 + w)\zeta')\bar{\Lambda}^* \right)}{(w+1)^2} k' \right. \\
&\quad + \frac{\epsilon_c (-1 + 2\zeta' + 2w(2 + w - 2\zeta' + 2w\zeta' + 2w^2\zeta'))\bar{\Lambda}}{(w+1)^2} k' \\
&\quad - \frac{\epsilon_c (3 + 3(-1 + 2w + w^2)\zeta')\bar{\Lambda}^*}{(w+1)^2} k' \\
&\quad + \frac{\epsilon_b \left(((1 + 6w + 6w^2 + 2w^3)\zeta')\bar{\Lambda} + (1 - 2\zeta')\bar{\Lambda}^* \right)}{(w+1)^3} k'^2 \\
&\quad + \frac{\epsilon_c \left((3 + 2(-2 + 3w + 3w^2 + w^3)\zeta')\bar{\Lambda} + (3 - 6\zeta')\bar{\Lambda}^* \right)}{(w+1)^3} k'^2 \\
&\quad \left. + \sum_{n=3}^m e_{n-1} k'^n + \mathcal{O}(k'^{(m+1)}) \right], \tag{109}
\end{aligned}$$

$$= g_+(w) + Z_{g_+}(w, k), \tag{110}$$

$$g_-(w') = g_-(w) + \zeta(1) \times [\zeta' k'], \tag{111}$$

$$= g_-(w) + Z_{g_-}(w, k), \tag{112}$$

with m some arbitrary order of the Taylor expansion, and the factor

$$e_n = \frac{(\epsilon_b + 3\epsilon_c)(2\zeta' - 1)(\bar{\Lambda} + \bar{\Lambda}^*)}{(w+1)^n}. \tag{113}$$

One identifies

$$Z_{f_+}(t, k) = -\frac{1}{2}\sqrt{m_B m_D} \left(\left(\frac{1}{m_B} + \frac{1}{m_{D_0^*}} \right) k_a Z_{g_+}^a(w, k) + \left(\frac{1}{m_B} - \frac{1}{m_{D_0^*}} \right) k_a Z_{g_-}^a(w, k) \right), \tag{114}$$

$$= k_a Z_{f_+}^a(t, k), \tag{115}$$

$$Z_{f_-}(t, k) = -\frac{1}{2}\sqrt{m_B m_D} \left(\left(\frac{1}{m_B} - \frac{1}{m_{D_0^*}} \right) k_a Z_{g_+}^a(w, k) + \left(\frac{1}{m_B} + \frac{1}{m_{D_0^*}} \right) k_a Z_{g_-}^a(w, k) \right), \tag{116}$$

$$= k_a Z_{f_-}^a(t, k). \tag{117}$$

C. Loop integrals

C.1. Passarino Veltman reduction of higher order tensor integrals

For one-loop tensor integrals a systematic algorithm has been worked out by Passarino and Veltman [26] to reduce any given higher-order tensor integral as a sum of four-vectors times scalar integrals. For integrals with one, two or three external legs we use the notation

$$A_{0,\mu\nu}(m^2) = \tilde{\mu}^{4-D} \int \frac{d^D k}{(2\pi)^{D/2}} \frac{1, k_\mu k_\nu}{(-k^2 + m^2)}, \quad (118)$$

$$B_{0,\mu,\mu\nu}(p^2; m_0^2, m^2) = \tilde{\mu}^{4-D} \int \frac{d^D k}{(2\pi)^{D/2}} \frac{1, k_\mu, k_\mu k_\nu}{(-k^2 + m_0^2) ((-p+k)^2 + m^2)}, \quad (119)$$

$$C_{0,\mu,\mu\nu}(p_1^2, s, p_2^2; m_0^2, m_1^2, m_2^2) = \tilde{\mu}^{4-D} \int \frac{d^D k}{(2\pi)^{D/2}} \frac{1, k_\mu, k_\mu k_\nu}{(-k^2 + m_0^2) ((-p_1+k)^2 + m_1^2) ((-p_2+k)^2 + m_2^2)}, \quad (120)$$

with an apparent generalization towards more external legs and higher rank tensor integrals. Note that we redefined $\tilde{\mu}^{4-D} = -i(4\pi)^2 \mu^{4-D}$ and skipped A_μ . The latter vanishes due to its odd transformation property when integrated. In addition we defined $s = (p_1 - p_2)^2$. Due to Lorentz symmetry the integration result can only depend on tensor structures from external momenta p_j^μ and the metric tensor $g^{\mu\nu}$. This implies

$$\begin{aligned} A^{\mu\nu} &= g^{\mu\nu} A_{00}, \\ B^\mu &= p^\mu B_1, \\ B^{\mu\nu} &= p^\mu p^\nu B_{11} + g^{\mu\nu} B_{00}, \\ C^\mu &= p_1^\mu C_1 + p_2^\mu C_2, \\ C^{\mu\nu} &= p_1^\mu p_1^\nu C_{11} + p_2^\mu p_2^\nu C_{22} + p_1^{[\mu} p_2^{\nu]} C_{12} + g^{\mu\nu} C_{00}. \end{aligned}$$

Contracting both sides of these equations with external momenta and the metric tensor yields a set of equations that allow the determination of the loop-form factors B_i, B_{ij}, C_i, C_{ij} with $i, j = 0, 1, 2$.

C.1.1. Derivatives of two-point functions

The derivative of a two-point function is defined as

$$\dot{B}_i = \frac{d}{dp^2} B_i(p^2; m_1^2, m^2), \quad (121)$$

with $i = 0, 1$.

References

- [1] N. Cabibbo, Phys. Rev. Lett. 10, 531 (1963).
- [2] J. Charles *et al.*, Eur. Phys. J. C 41, 1 (2005).
- [3] M. Bona *et al.*, JHEP, 0603:080 (2006).
- [4] S. Weinberg, Phys. Rev. 140, 516 (1965).
- [5] D.R. Yennie, S.C. Frautschi, and H. Suura, Ann. Phys. 13, 379452 (1961).
- [6] A. Sirlin, Revs. Mod. Phys. 50, 573 (1978).
- [7] A. Sirlin, Nuc. Phys. B, 196, 83 (1982).
- [8] S. Eidelman *et al.*, Phys. Lett. B 592, 1 (2004).
- [9] A. Sher *et al.*, Phys. Rev. Lett. 91, 261802 (2003).
- [10] T. Alexopoulos *et al.*, Phys. Rev. Lett. 93, 181802 (2004).
- [11] T. Alexopoulos *et al.*, Phys. Rev. D 70, 092006 (2004).
- [12] T. Alexopoulos *et al.*, Phys. Rev. D 70, 092007 (2004).
- [13] E. Barberio, B. van Eijk, and Z. Was, Comput. Phys. Commun. 66,115 (1991).
- [14] E. Barberio and Z. Was, Comput. Phys. Commun. 79, 291308 (1994).
- [15] T.C. Andre, Nuc. Phys. B, Vol. 142, 58-61 (2005).
- [16] C. Gatti, Eur. Phys. J. C 45, 417 (2006).
- [17] E.S. Ginsberg, Phys. Rev., 142, 4 (1966).
- [18] E.S. Ginsberg, Phys. Rev., 171, 5 (1968).
- [19] E.S. Ginsberg, Phys. Rev. D, 1, 1 (1970).
- [20] W. Pauli and F. Villars, Rev. Mod. Phys, 21, 434-444 (1949).
- [21] J.C. Ward, Phys. Rev. 79, 182 (1960).
- [22] F.E. Low, Phys. Rev. 100, 974 (1958).
- [23] T.H. Burnett and N.M. Kroll, Phys. Rev. Lett. 20, 86 (1968).
- [24] H. Fearing *et al.*, Phys. Rev. D, 2, 3 (1970).
- [25] H. Fearing *et al.*, Phys. Rev., 184, 5 (1969).
- [26] G. Passarino and M.J.G. Veltman, Nucl. Phys. B 160, 151, (1979).
- [27] T. Hahn and M. Perez-Victoria, Comput. Phys. Commun. 118, 153 (1999).
- [28] W.H. Press *et al.*, Numerical Recipes in Fortran, Cambridge University Press, Second Edition (1992).
- [29] <http://slac.stanford.edu/~florian/blur/>
- [30] C. Amsler *et al.*, Phys. Lett. B 667, 1 (2008).
- [31] M. Schoenherr and F. Krauss, JHEP 0812, 018 (2008).
- [32] F. Bernlochner and Marek Schönherr, to be published.

- [33] I. Caprini, L. Lellouch, and M. Neubert, Nucl. Phys. B, 530, 153 (1998).
- [34] HFAG update from ICHEP08 results: <http://www.slac.stanford.edu/xorg/hfag/semi/ichep08/home.shtml>
- [35] P. Ball and R. Zwicky, Phys. Rev. D, 71, 014015, (2005).
- [36] A.K. Leibovich, Z. Ligeti, I.W. Stewart, and M.B. Wise, Phys. Rev. Lett. 78, 3995 (1997).
- [37] A.K. Leibovich, Z. Ligeti, I.W. Stewart, and M.B. Wise, Phys. Rev. D57, 308 (1998).
- [38] N. Isgur and M.B. Wise, Phys. Lett. B 232, 113 (1989); B 237, 527(1989).